On the vertical structure and stability of the Lofoten vortex in the Norwegian Sea

I.L. Bashmachnikov[1,2,3] [1], *M.A. Sokolovskiy*[4,5], *T.V.Belonenko*[2], *D.L. Volkov*[6,7], *P.E. Isachsen*[8,9] *and X. Carton*[10]

[1] NIERSC- Nansen International Environmental and Remote Sensing Centre, 14th line, St. Petersburg, Russia;

[2] the St. Petersburg State University, Department of Oceanography of the Institute of Earth Science, 7/9 Universitetskaya nab., St. Petersburg, 199034, Russia.;

[3] Previously: MARE – Marine and Environmental Sciences Centre, Faculdade de Ciências, Universidade de Lisboa, Campo Grande, 1749-016 Lisboa, Portugal;

[4] Water Problems Institute, Russian Academy of Sciences, Moscow, 119333, Russia;

[5] P.P. Shirshov Institute of Oceanology, Russian Academy of Sciences, Moscow, 117997, Russia;

[6] Cooperative Institute for Marine and Atmospheric Studies, University of Miami, Miami FL, USA;

[7] NOAA Atlantic Oceanographic and Meteorological Laboratory, Miami FL, USA;

[8] Department of Geosciences, University of Oslo, Oslo, Norway;

[9] Norwegian Meteorological Institute, Oslo, Norway;

[10] Laboratoire de Physique des Océans, UMR 6523, Université de Bretagne Occidentale, 6 avenue Le Gorgeu, 29200 Brest, France.

Abstract

The Lofoten Vortex (LV), a quasi-permanent anticyclonic eddy in the Lofoten Basin of the Norwegian Sea, is investigated with an eddy-permitting primitive equation model nested into

---

[1] Corresponding author:
E-mail address: igorb1969@mail.ru (I.L. Bashmachnikov);
1 NIERSC- Nansen International Environmental and Remote Sensing Centre, 14th line, St. Petersburg, Russia.
2 Department of Oceanography at the Institute of Earth Science of the St. Petersburg State University (SPbSU), 7/9 Universitetskaya nab., St. Petersburg, 199034, Russia;
3 MARE – Marine and Environmental Sciences Centre, Faculdade de Ciências, Universidade de Lisboa, Campo Grande, 1749-016 Lisboa, Portugal;

the ECCO2 ocean state estimate. The LV, as simulated by the model, extends from the sea surface to the ocean bottom at about 3000 m and has the subsurface core between 50 m and 1100 m depths. Above and below the vortex core the relative vorticity signal decreases in amplitude while the radius increases by as much as 25-30% relative to the values in the core. Analyzing the model run, we show that the vertical structure of the LV can be casted into four standard configurations, each of which forms a distinct cluster in the parameter space of potential vorticity anomalies in and above the LV core. The stability of the LV for each of the configurations is then studied with three-layer and a two-layer (in winter) quasi-geostrophic (QG) models over a flat bottom as well as over a realistic topography. The QG results show a number of common features with those of the primitive equation model. Thus, among the azimuthal modes dominating the LV instability, both the QG model and the primitive equation model show a major role the 2nd and 3rd modes. In the QG model simulations the LV is the subject of a rather strong dynamic instability, penetrating deep into the core. The results predict 50-95% volume loss from the vortex within 4-5 months. Such a drastic effect is not observed in the primitive equation model, where, for the same intensity of perturbations, only 10-30% volume loss during the same period is detected. Taking into account the gently sloping topography of the central part of the Lofoten basin and the mean flow in the QG model, brings the rate of developpmet of instability close to that in the primitive equation model. Some remaining differences in the two models are discussed. Overall, the LV decay rate obtained in the models is slow enough for eddy mergers and convection to restore the thermodynamic properties of the LV, primarily re-building its potential energy anomaly. This justifies the quasi-permanent presence of the LV in the Lofoten Basin.

Keywords: Lofoten vortex, vertical structure, vortex stability, primitive equation model, QG model.

1. Introduction

The Lofoten Basin is a bowl-shape depression in the bottom topography of the Norwegian Sea (68 - 72 °N and 2 °W - 10 °E) with a maximum depth of about 3250 m. It is located between the Mohn Ridge (about 2000 m deep) to the northwest and the Scandinavian Peninsula to the east, and is limited in the south by the Jan-Mayen Fracture zone (about 2000 m deep) and the north-western flank of the Voring plateau (Fig. 1).

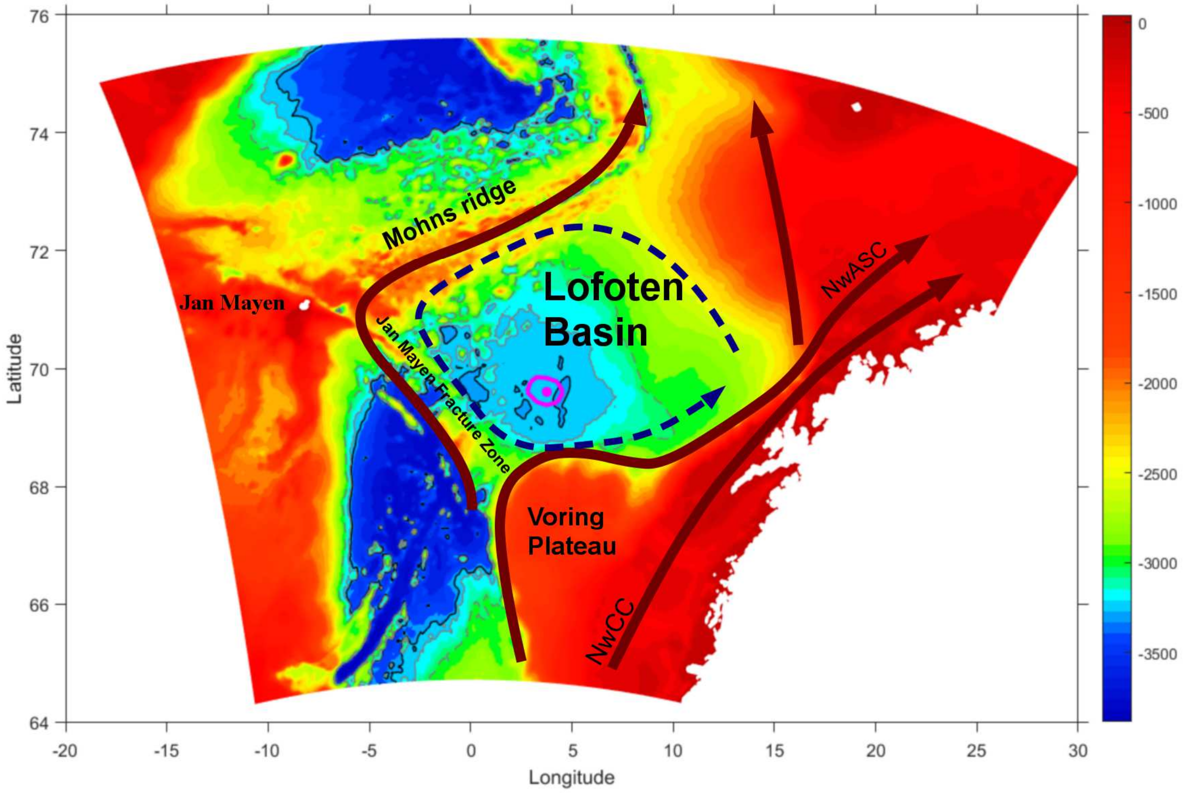

Fig. 1. Topographic map of the Lofoten Basin (depth in m) with the major flows overlaid. One minute GEBCO topography is used. Gray dashed contours mark 3000 m, gray solid contours – 3200 m and solid black contours – 3250 m depth. Surface and deep currents are sketched with dark red and blue lines, respectively. The magenta dot in the center of the LB is the most frequent position of the Lofoten Vortex (LV). The magenta line around the dot limits the area where the LV center is observed 80% of time for the 15 years of simulations with MIT GCM. NwASC is the Norwegian Atlantic Slope Current, NwCC is the Norwegian Atlantic Coastal Current.

Warm and salty Atlantic Water (AW) occupies the upper 800-1000 m of the Lofoten Basin. The AW overlies denser waters of both lower temperatures and salinities (Blindheim and Rey, 2004; Nilsen and Nilsen, 2007). In the AW layer, temperature and salinity both increase towards the center of the basin (Boyer et al., 2005), while the density surfaces at mid-depths are bent down as much as 300 m over the center of the Lofoten Basin and towards the Lofoten Islands relative to the northwestern and the southwestern basin boundaries (Rossby et al., 2009). Being the major heat reservoir in the Nordic Seas, this is a region of strong atmosphere–ocean interactions. It is also a region of intense mesoscale dynamics which impacts the net warm water flux to the Arctic, making it a sub-Arctic "hot spot" of ocean variability (Volkov et al., 2013).

The Norwegian Atlantic Current (NwAC) dominates the near-surface circulation along the eastern rim of the Norwegian Sea and brings the warm and salty AW north at an average velocity of 20-30 cm s^{-1} (Blindheim and Rey, 2004, Koszalka et al., 2011, Lumpkin and Johnson, 2013; Volkov et al., 2015). The NwAC consists of a topographically controlled near-barotropic current flowing along the shelf break of the Scandinavian Peninsula and a strongly baroclinic jet that follows 2000-2500 m isobaths, the Norwegian Atlantic Slope Current (NwASC) (Koszalka et al., 2011; Volkov et al., 2015). Instability of the NwAC is considered to be the main source of the intense mesoscale variability in the Lofoten Basin. Results of a two-layer model (Orvik, 2004) and further observations (Blindheim and Rey, 2004, Gascard and Mork, 2008, Koszalka et al., 2011, Lumpkin and Johnson, 2013) also revealed a northward surface current along the Mohn Ridge, at the western edge of the Lofoten Basin, with a mean velocity of 10-15 cm s^{-1}.

At depth, an overall bottom-intensified cyclonic gyre around the Lofoten Basin was detected in a diagnostic regional circulation model (Nøst and Isachsen, 2003) and in analyses of Argo float trajectories (Poulain et al., 1996; Jakobsen et al., 2003; Orvik, 2004). The velocity, estimated from ARGO float trajectories is 5-10 cm s^{-1} (Gascard and Mork, 2008). It has been suggested that the cyclonic gyre is a bottom-trapped branch of the deeper fractions of the NwASC, maintained by eddy transport of the warm and salty AW into the Lofoten Basin and its further downwards penetration by vertical diffusion (Ivanov and Korablev, 1995a,b; Pereskokov, 1999; Orvik, 2004).

Russian hydrographic surveys in the 1970s and 1980s discovered a quasi-permanent anticyclonic vortex in center of the Lofoten Basin, named the Lofoten Vortex (hereafter LV, Ivanov and Korablev, 1995a,b). The vortex is located at around 70° N, 2° E, has a diameter of about 60-80 km, and is characterized by positive temperature and salinity anomalies between 400 and 2000 m depths (Fig. 2, see also Alexeev et al., 1991; Pereskokov, 1999) with the strongest signal found at around 800 m (Alexeev et al., 1991; Romantcev, 1991). The existence of the LV was later confirmed by trajectories of neutrally-buoyant floats and surface drifters (Søiland et al., 2008; Koszalka et al., 2011). Ivanov and Korablev (1995b) suggested that the LV stays at approximately the same position in the center of the Lofoten Basin due to its interaction with the mean bottom-intensified cyclonic gyre or, since the LV extends throughout the entire water column, with the bowl-shaped topography itself (Raj et al., 2015).

Repeated oceanographic surveys from 1985 to 1991 (Ivanov and Korablev, 1995a) show that the LV thermohaline anomalies strengthen in winter and spring. This is accompanied by a reduction of the LV radius and a strengthening of its maximum anticyclonic rotation velocity. Based on these observations, Ivanov and Korablev (1995a) suggested that the LV regenerates periodically due to anomalously strong convective mixing over its core in winter. The seasonality itself has later been confirmed in eddy-resolving primitive equation simulations and in altimetric observations by Köhl (2007) and Raj et al. (2015). However, these authors attributed the regeneration not primarily to winter convection but rather to the merger of the LV with other anticyclones in the basin. In fact, drifter trajectories and satellite altimetry have confirmed a higher level of eddy activity in the Lofoten Basin in winter and spring (Köhl, 2007; Søiland et al., 2008; Koszalka et al., 2011). Both cyclones and anticyclones appear to originate from instability of the Norwegian current near the Lofoten Islands (Søiland et al., 2008; Koszalka et al., 2011). Thus, Isachsen (2015) used time-averaged fields of an eddy-resolving numerical ocean simulation to calculate linear growth rates and corresponding length scales based on linear quasi-geostrophic (QG) vertical mode equations. The fastest unstable growth was found along the steepest part of the continental slope off the Lofoten-Vesteraalen islands. The current flowing the Mohn Ridge was also found to be unstable, but with lower growth rates. Steered by the bowl-shaped topography of the Lofoten Basin, some of the anticyclones generated in the boundary currents eventually approach and merge with the LV.

So both eddy mergers and winter convection appear to strengthen this vortex. But the observed quasi-permanent state of the LV must ultimately reflect a long-term balance between re-generation and dissipation (or break-up) processes. As outlined above, the first process has been studied to some degree. The second process, decay of the LV, has not received similar attention and is therefore the main focus of this paper.

Mesoscale vortices, like the LV, can in principle decay due to small-scale turbulent diffusion and to instability triggered by external perturbations. However, since such vortices are typically surrounded by strong potential vorticity (PV) gradients (Hua et al., 2013; Bashmachnikov et al., 2015), turbulent diffusion is suppressed. In the case of the LV a decay time due to the effect of turbulent diffusion has been estimated to be dozens of years (Søiland and Rossby, 2013). In contrast, hydrodynamic instability of the vortex itself could be an efficient decay mechanism (Smeed, 1988b; Rishardson et al., 2000; Bashmachnikov et al., 2015).

A baroclinic vortex is subject to four main types of instability (Ripa, 1992; Cushman-Roisin and Beckers, 2011): baroclinic instability (due to coupling of Rossby waves), hybrid and Sakai instabilities (due to coupling of Rossby waves with frontally-trapped inertia-gravity waves), Kelvin-Helmholtz instability (due to coupling between inertia-gravity waves) and barotropic instability (Rossby waves are sustained by a horizontal shear of the mean flow). Kelvin-Helmholtz and Sakai instabilities are developed only at much higher Rossby numbers (Ro) than observed in the LV. For low Rossby numbers and low ratio of vortex-core thickness to water depth, hybrid and baroclinic instabilities may be generated. As the ratio of vortex-core thickness to water depth decreases the instabilities develop at a progressively slower rate (Ripa, 1992; Cohen et al., 2015a).

In two-dimensional incompressible and inviscid fluids, a circular vortex with uniform relative vorticity (a Rankine vortex), which is a stationary solution of the Euler equations, is stable to small-amplitude perturbations on its contour (Lamb, 1885). This result also holds for a two-dimensional vortex with uniform PV in a rotating environment, but it does not hold for a baroclinic vortex in the ocean. Quite simply, in a two-layer fluid (the simplest approximation of a baroclinic system) the Rankine vortex may become unstable if the sign of the PV changes from one layer to another (Pedlosky, 1985; Kozlov et al., 1986; Flierl, 1988; Helfrich and Send, 1988). The instability theory for two-layer vortices was further developed, in particular, in the works by Sokolovskiy (1988), Paldor and Nof (1990), Ripa (1992), Mesquita and Prahalad (1999), Sokolovskiy and Verron (2000), Benilov (2000, 2001, 2003, 2004, 2005a, 2005b), Thivolle-Cazat et al (2005), Reinaud and Carton (2009), Sokolovskiy et al (2010), Carton et al. (2010a,b), Makarov et al. (2012), Cohen et al. (2015), Cohen et al. (2016).

Similar arguments apply in the three-layer model (Holmboe, 1968; Davey, 1977; Wright, 1980; Smeed, 1988a, 1988b; Sokolovskiy, 1991; Ikeda, 1993). A sufficient condition for instability is achieved when at least one of the stratification parameters, γ_1 or γ_2 (inversely proportional to the first and the second Rossby radii of deformation, respectively, - see Appendix A), reach a certain threshold value (Sokolovskiy, 1997a, 1997b). Smeed (1988a, 1988b) has shown that for typical upper ocean conditions, when the density jump across the lower interface ($\Delta\rho_2$ - between layers 2 and 3) is much less than that across the upper interface ($\Delta\rho_1$ - between layers 1 and 2), the instability develops as long waves generated at the sloping isopycnal above the eddy core (the interface between layers 1 and 2), and short waves generated at the sloping isopycnal below the eddy core (the interface between layers 2 and 3). This result was theoretically and numerically confirmed by Sokolovskiy (1997a, 1997b) for a “cylindrical” vortex in a three-layer fluid, as well as for a “cone-shaped” three-layer vortex (i.e. when the initially circular vortex patches have different radii in different layers).

Thus, stability analyses of circular geostrophic vortices give evidence that the nonlinear evolution of such vortices can lead to a break-down of an initially monopolar vortex into multiple structures (Pedlosky, 1985; Kozlov et al., 1986; Flierl, 1988; Helfrich and Send, 1988; Sokolovskiy, 1988, Carton and McWilliams, 1988; Carton and Corréard, 1999). Applications of the theoretical results to real ocean data suggest that most vortices should be unstable (e.g., Ikeda 1981; Flierl, 1988; Helfrich and Send, 1988; Carton and McWilliams 1989; Ripa 1992; Killworth et al., 1997; Benilov et al., 1998; Baey and Carton, 2002; Benilov, 2003; Katsman et al., 2003). Observations, in contrast, indicate that ocean vortices often persist for years (e.g., Lai and Richardson, 1977; Bashmachnikov et al., 2015). A promising attempt to solve this apparent contradiction was made by Dewar and Killworth (1995), who considered a Gaussian vortex in the upper layer and a relatively weak co-rotating circulation in the lower layer in a two-layer shallow-water model. It was found that the deep flow can stabilize the eddy or, at least, weaken its instability considerably. This idea was further developed by Benilov (2004), who demonstrated that the deep flow, corresponding to a uniform PV in the lower layer, stabilizes all types of vortices, not only the Gaussian one. Benilov (2004) thus argued that non-zero deep flows are a common feature for long-lived oceanic eddies.

The Lofoten Vortex is long-lived vortex; this is an observational fact. A first explanation of its dynamic stability was offered by Köhl (2007). Building his results on a 2-layer study by Benilov (2005a), the author argued that the LV may be stabilized by a 100-m bowl-shaped depression of the bottom topography. This explanation is questionable since it would only apply for a first baroclinic Rossby radius of deformation in the Lofoten Basin being several times larger than actually observed. Also, as is shown in Fig.1 and Fig.2, most of the time the LV center is situated not over a bottom depression, but is rather surrounded by a set of small depressions, while high-gradient bowl-shape basin boundaries are separated from the LV center by a distance of several vortex radii.

It is more likely that PV gradients between the LV core and the surrounding ocean determine its stability characteristics. Thus, the LV decay has to be studied in terms of barotropic or baroclinic instability. For such investigation a detailed knowledge of the horizontal and vertical structure of the LV is critical. Previous studies of remote sensing and model data have given a relatively good picture of the horizontal structure of the LV near the surface and its time variability (Köhl, 2007; Soiland and Rossby, 2013; Volkov et al., 2015). The vertical structure of the vortex, studied so far only from scattered in-situ observations (Ivanov and Korablev, 1995a,b; Blindheim and Rey, 2004; Gascard and Mork, 2008; Soiland and Rossby, 2013; Raj et al., 2015), is less well known. As outlined above, knowledge of this vertical structure, however, is key for an understanding of the vortex stability. A closer look at the vertical structure of the LV is, therefore, also a focus of this study.

The paper is structured as follows. An overview of data and methods is given in Section 2. The following section begins by describing the vertical structure of the LV, as obtained in eddy-permitting primitive equation simulations nested into the global ECCO2 state estimate. This includes a discussion of the time evolution of the main vortex parameters and a classification of the LV PV states in selected vertical layers (Sections 3.1-3.3). These results are then used to study the stability of the LV in a 3-layer QG model, both in the linear and nonlinear regimes (Section 3.4), and also including the effects bottom slope and a background current (Section 3.5). Finally, temporal variability of the LV in the primitive equation model is diagnosed and compared with the predictions of the stability calculations (Section 3.6). In Section 4 we summarize and discuss the results.

2. Data and Methods:

2.1 Primitive equation model

Eddy-permitting numerical experiments of the Lofoten Basin and surrounding ocean regions (see Fig. 1) have been performed with the Massachusetts Institute of Technology primitive equation model (MIT GCM, Marshall et al., 1997) nested into the ECCO2 (Estimating the Circulation and Climate of the Ocean, Phase 2; http://ecco2.jpl.nasa.gov) ocean state estimate of the North Atlantic and the Arctic Ocean (Nguyen et al, 2011). ECCO2 is an accurate, physically consistent, time-evolving synthesis of the ocean circulation by a least square fit of full-depth ocean and sea ice dynamics to selected satellite and in situ data. The eddy-permitting regional model used for this study adopts the parameter set (surface heat and momentum fluxes, vertical mixing coefficients, etc.) obtained in the optimized ECCO2 model. The nested model run is integrated using a finite volume discretization with C-grid staggering of the prognostic variables and has a horizontal mesh-size of around 4x4 km in the Lofoten Basin. Given a first baroclinic Rossby radius of deformation of 7-8 km (Nurser and Bacon, 2014) in the region and a radius of the LV itself of about 30 km, the nested model is hence eddy-permitting. The model has 50 vertical z-levels, their mean thickness ranging from 10 m in the upper ocean to 456 m below 2000 m.

The General Bathymetric Charts of the Oceans (GEBCO) with one arc-minute grid (Smith and Sandwell, 1997) is used as bottom topography. The partial cell formulation (Adcroft et al., 1997) allows for an accurate representation of the bathymetry in the model. The computations were started from rest, using climatological temperature and salinity from the World Ocean

Atlas 2009 (WOA09) (Locarnini et al., 2010; Antonov et al., 2010). Over the 1992-2013 period, the simulations were forced with a 6-hourly atmospheric state obtained from the 25-year Re-Analysis of the Japan Meteorological Agency (JRA25-JMA) with the original 1.25x1.25 degree spatial resolution. Lateral boundary conditions are taken from ECCO2 simulations. Time-mean fields used in this paper are taken from the 1995–2010 time period, leaving the first years for model spin-up. Further details on the model description and set-up are given in Losch et al. (2010), Nguyen et al. (2011) and Volkov et al. (2015).

Analysis of variations of the LV near-surface mean relative vorticity in the MIT GCM and satellite altimetry observations (Ray et al., 2015; Volkov et al., 2015) showed that the model adequately describes seasonal and interannual variations in the LV dynamics at the sea-surface. The model was also shown to adequately reproduce other details of large-scale and mesoscale dynamics in the Lofoten Basin, as reported by a number of observational studies (see, for example, Blindheim and Rey, 2004, Gascard and Mork, 2008, Koszalka et al., 2011, Lumpkin and Johnson, 2013).

2.2 Algorithm for obtaining characteristics of the LV

Our study is based on weekly 3D fields of the primitive equation model temperature, salinity and velocity. The LV is identified at the centre of the Lofoten Basin by the deep penetration of its temperature and salinity anomalies (Fig. 2), as well as its relative vorticity signature. The analyses are done in a reference frame following the vortex, so consecutive positions of the LV were tracked using the peak negative relative vorticity at 700 m depth. The level chosen assures higher stability of the tracking algorithm, as the peak relative vorticity anomaly of the LV core at this level nearly always exceeds the corresponding anomalies of surface-intensified anticyclonic eddies propagating into the basin from the NwAC. Specifically, every new position of the LV was defined from the minimum of relative vorticity within a 40-km large disk (slightly larger than the typical LV radius defined by Köhl, 2007), from the vortex position at the previous step. To cope with the situations where the LV centre has drifted by more than one LV radius after a week, the algorithm undergoes three iterations for every time step, each one starting with the newly defined position of the minimum of relative vorticity. This “creeping” technique allows fixing the LV centre, separated by up to three LV radii from its previous position (this covers the possibility of LV translation at unrealistic velocities of 20 cm s^{-1}). The procedure simultaneously avoids unwanted jumps of the LV position to the centre of a neighboring anticyclone, which happens to have a stronger instantaneous relative vorticity anomaly. The robustness of the algorithm was verified by visual inspection of subsequent vorticity fields. The results show that the main LV core forms the strongest relative vorticity anomaly even when secondary vortices are separated from its skirt.

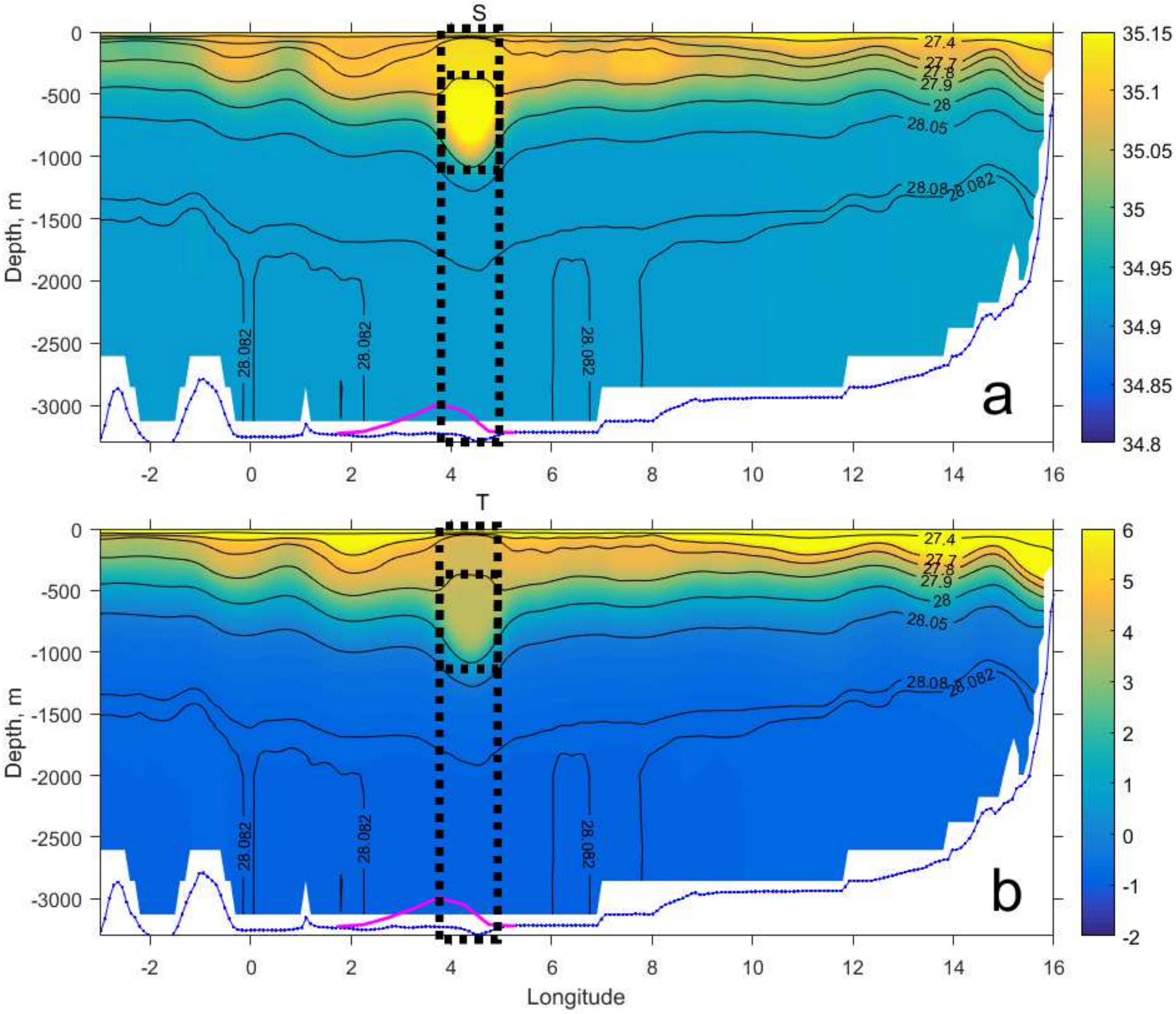

Fig. 2. A section of salinity (a) and of temperature (°C, b) across the center of the Lofoten Vortex (69.7°N) at 24.08.2005 in the MIT GCM simulations. Thin isolines mark potential density surfaces referenced to 500 m depth. The LV position and the mean depths of the 3 layers used for stability analysis are marked with dashed rectangles. GEBCO topography, interpolated to the model grid, limit the data distribution from below (blue line). Magenta lines mark the frequency of observation of the LV center along this section (out of scale, the line edges mark zero number of observations).

With the LV position identified, the vortex extent was deduced from its relative vorticity field. Relative vorticity profiles were derived along rays, originating from the LV centre and covering an ellipse with 10° increments (Fig. 3). Along each profile, the LV dynamic radius was defined using two complementary algorithms. In the first algorithm, the radius was defined as the minimum distance along each ray at which either 1) the relative vorticity profile crosses zero, or 2) the relative vorticity has a local maximum, or else 3) the rate of decrease of the relative vorticity slows down significantly (below 25% of its maximum rate along the ray). The latter two criteria help to avoid situations when the LV core extends across connected filaments. In the second algorithm only the first criterion was used. At times, special vorticity configurations were the LV center is fully circled by two nested rings of higher and then lower relative vorticity were identified (Fig. 3c). Those situations usually take place immediately after a full or partial merger of a surface anticyclone with the LV. In these cases the LV radius was defined using the second algorithm.

Having collected the points of the LV boundary, the position of the LV centre was refined (from the first guess given by the tracking algorithm) as the algebraic mean of the boundary coordinates. The LV mean radius was further defined as the mean distance from the refined centre of the LV and the LV boundary points. The maximum and minimum radii were obtained via a robust least-square fit of the boundary points to an ellipse (Fig. 3).

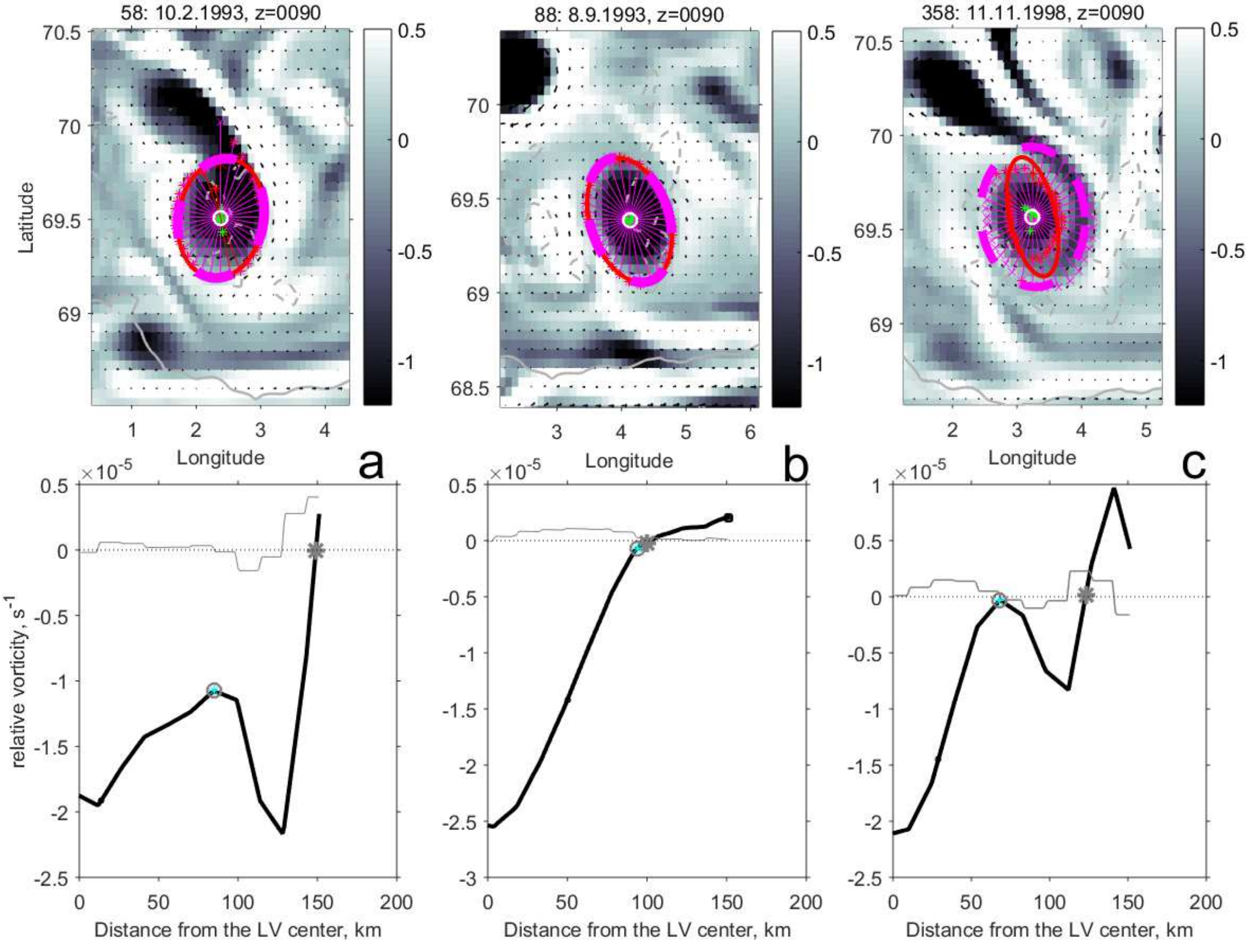

Fig. 3. Upper panels: relative vorticity distribution at 100 m depth (x10^{-5} s^{-1}). Red and magenta lines connect the LV centre and the LV boundaries in radial directions. Lower panel: sampled profiles of relative vorticity for the distributions above, running from the LV center northwards. (a) – 10.02.1993; (b) – 08.09.1993; (c) – 11.11.1998. Red ellipse (upper plots) and empty circles (lower plots) mark the LV boundary defined with the first algorithm (as described in the text); dashed magenta ellipse (upper plots) and grey stars (lower plots) mark the boundary defined with the second algorithm (as described in the text).

2.3 Constructing a 3-layer isopycnal model

To study the vertical structure of the vortex in an isopycnal framework, potential density surfaces referenced to 500 m ($\sigma_{0.5}$) were computed with an increment of 0.02 kg m^{-3}. The bulk of the analysis to follow assumes a 3-layer structure of the vortex. Further, in Section 3.2, it will be shown that the LV represents an S-vortex in the classification of Morel and McWilliams (1997). For such vortices, negative potential vorticity anomalies of the vortex core are vertically constrained with positive potential vorticity anomalies above and below the core, resulting from compression of isopycnals (see Figs. 4 and 5). Having this in mind, the isopycnals that separate the water column into three layers (with the second layer constituting the vortex core) were defined using two other sets of reference isopycnals. The first set was taken as the two isopycnals that show the maximum deflection above and below the LV center from their mean position outside the vortex. Those isopycnals are thus within the weakly-stratified core of the LV. The second set was taken from the isopycnals that experience the strongest squeezing above and below the core, i.e. the two isopycnals that have the smallest ratio of the distances to the neighboring isopycnals over the LV center to the mean distances between the same isopycnals. Finally, the two isopycnals limiting the core from above and from below were selected as those at mid-distance between the two sets defined above.

With the two isopycnals separating the three layers identified, mean isopycnal depths were calculated. Deflections of the isopycnals in the LV (η_1 and η_2) were then computed as the differences between the isopycnal depth in the LV center and the mean depth of the same isopycnal in an extended region around the LV.

3. Results

3.1 The vertical structure of the LV

Figure 4 shows typical horizontal maps and vertical sections of relative vorticity across the LV. The relative vorticity anomaly shows up as a columnar pattern which reaches the ocean bottom. However, the vorticity intensity sharply decreases and the vortex radius increases below 1000 m depth.

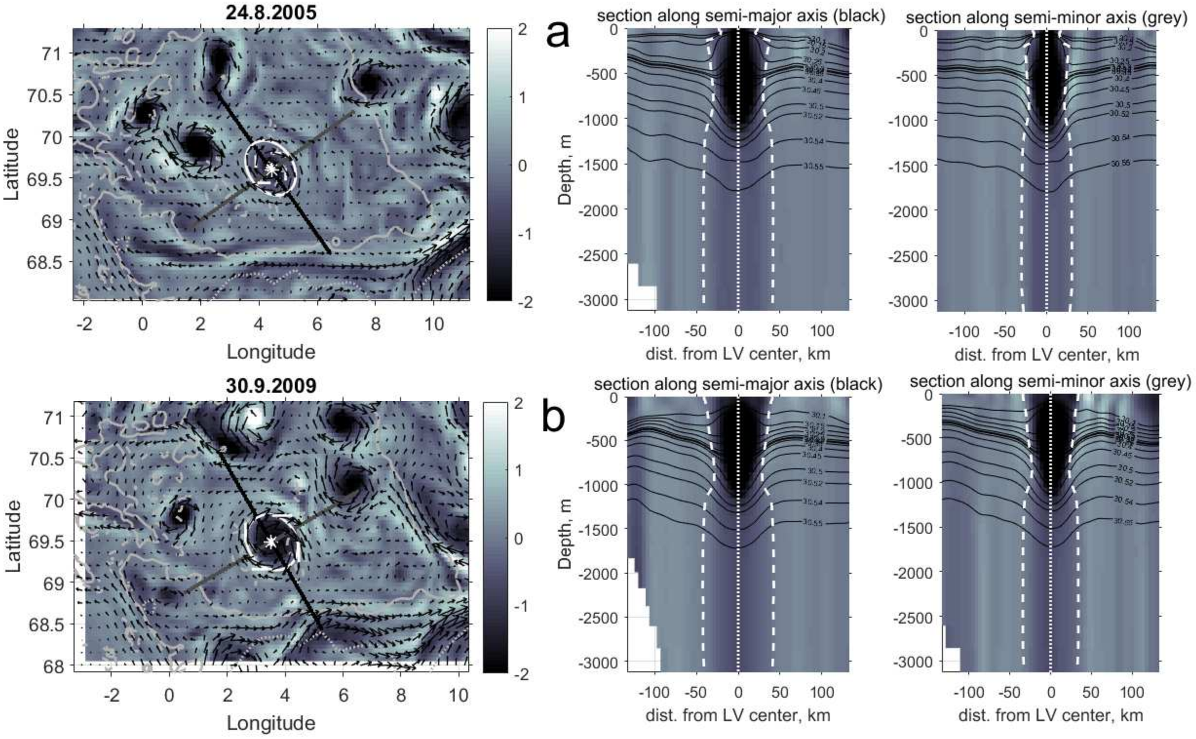

Fig. 4. Horizontal maps at 100 m depth (left-hand panels) and vertical profiles (middle and right-hand panels) of relative vorticity (x10^{-5} s^{-1}) in the Lofoten Basin: a- 24.08.2005; b- 13.09.2009. In the horizontal maps horizontal velocity vectors are overlaid; black and grey lines mark the position of vertical section along the LV semi-major and semi-minor axes of the approximating ellipse, respectively. The vertical sections show cuts along the semi-major axis (middle panels) and semi-minor axis (right-hand panels) of the vortex. In the vertical sections solid black isolines are $\sigma_{0.5}$ and vertical white dotted and dashed lines mark the LV axis and boundaries (dynamic radii), respectively.

Time-averaged vertical profiles of selected geometric and dynamic characteristics of the LV are presented in Figure 5. The LV azimuthal velocity, the relative vorticity and the dynamic radius reach their peak values at 500-600 m, 700-800 m and 800-900 m, respectively. The 200-800 m layer is also characterized by the strongest temperature-salinity anomaly (see also Fig. 2), as well as by the peak negative Ertel PV anomaly. Ertel PV is defined as $\Pi_E = N^2(f + \omega)/g$, where N is the buoyancy frequency, f is Coriolis parameter, ω is the mean relative vorticity of the LV core at a depth level and g is the gravitational acceleration. Ertel PV anomaly is defined as the difference between Ertel PV in the LV center and in the surrounding ocean.

Figure 5 (as well as Figs. 2 and 4) shows that the LV core is intensified below the sea-surface. This suggests that the LV vertical structure can be split in 3 layers. The upper layer (layer 1), above the LV core, extends on average from the sea-surface to 50-200 m. In this layer, the LV radius (R) increases with depth. The core layer (layer 2) extends from 50-200 m to 900-1100 m and is characterized by overall peak dynamic properties, as described above. In particular, the peak relative vorticity anomaly is between $-2\text{x}10^{-5}$ and $-3\text{x}10^{-5}$ s^{-1}. R in the layer decreases with depth down to a minimum of about 25 km at around 900 m. The lower layer (layer 3), from 900-1100 m to the ocean bottom, is characterized by a more than a five-fold decrease of relative vorticity (as compared to its peak value in layer 2) and by a larger R of around 35 km.

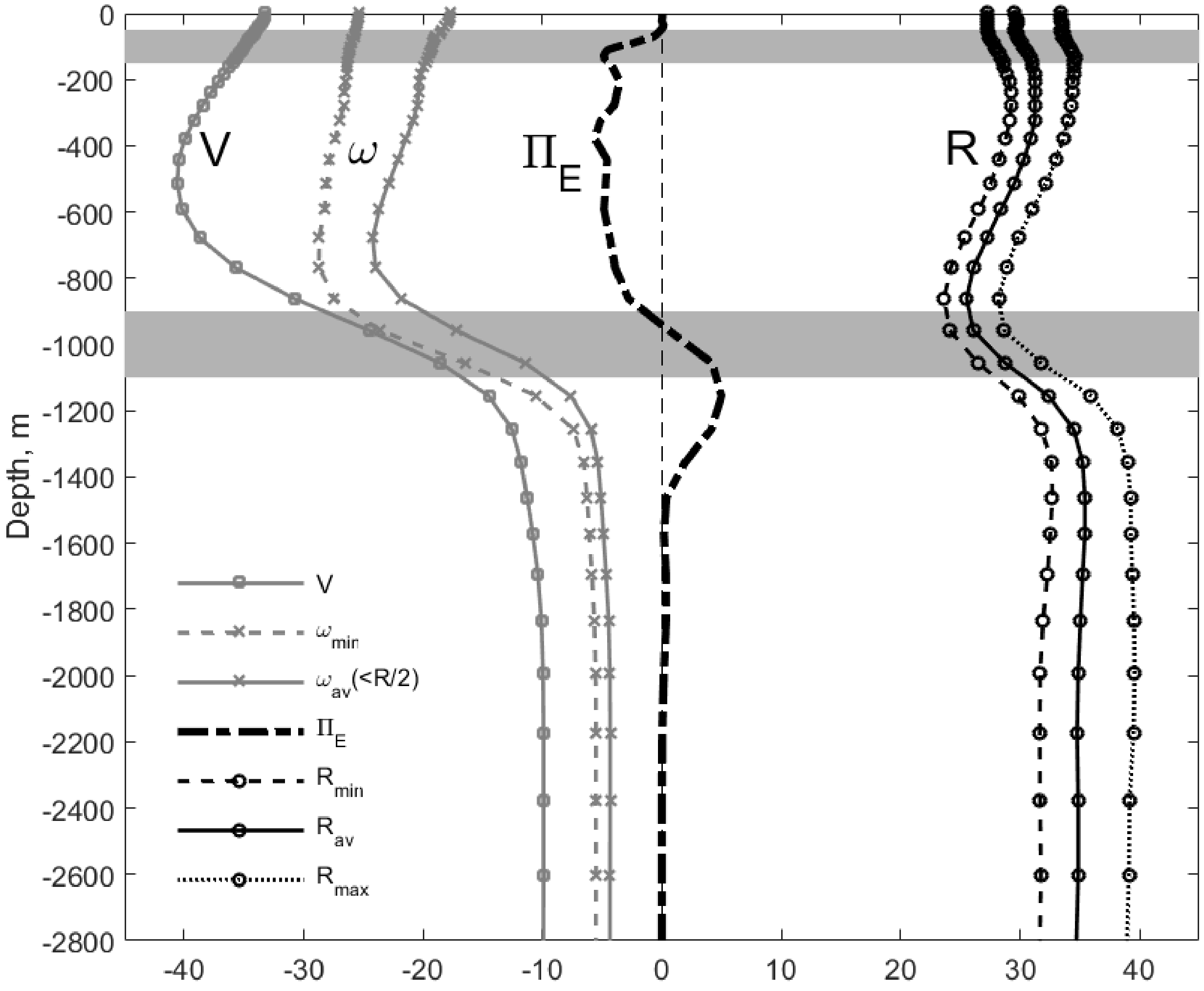

Fig. 5. Vertical profiles of selected time-mean characteristics of the LV (from 1998 to 2012): black lines with circles are dynamic radii (km) – the mean radius (solid line - R_{av}), the lengths of the semi-minor axis (dashed line - $R_{\min}$) and of the semi-major (dotted line - $R_{\max}$) axis; thick grey lines with crosses are relative vorticity profiles (10^6 s^{-1}) – the peak (solid line - ω_{min}) and averaged in the disk with the radius $R_{av}/2$ (dashed line - ω_{av}), thick gray line with squares is the maximum azimuthal velocity (V , cm s^{-1}); black dash-dot line is profile of Ertel potential vorticity anomaly in the LV center (Π_E, 10^{11} s^{-1}). Gray horizontal bands present approximate positions of the time mean upper and lower boundaries of the LV core.

3.2 Time evolution of the LV parameters

In this section, the time evolution of the vertical structure and of the horizontal geometry of the LV, in a 3-layer isopycnal framework (Section 2.3), is considered. The time evolution of the mean layer thicknesses outside the LV, the layer thicknesses in the LV itself and layer deflections at the LV center (η_1 and η_2) are presented in Fig. 6. The strong variability of the depth of the upper layer has both seasonal and interannual pattern. During some years winter convection penetrates into the LV core, and layers 1 and 2 merge for a couple of months, until the late spring re-stratification of the upper ocean restores the 3-layer structure of the LV. Figure 7 shows the evolution of the layer-averaged temperatures and potential densities referenced to 500 m depth ($\sigma_{0.5}$) in the LV. Seasonal fluctuations reach layer 2 although strongly reduced in amplitude. Both Figs. 6 and 7 show that the first simulation years are characterized by a noticeable evolution of the LV parameters, from which we conclude that the LV structure is not fully developed in the model until about 1998. Our further analyses the LV dynamics will therefore be based on the period from 1998 to 2012.

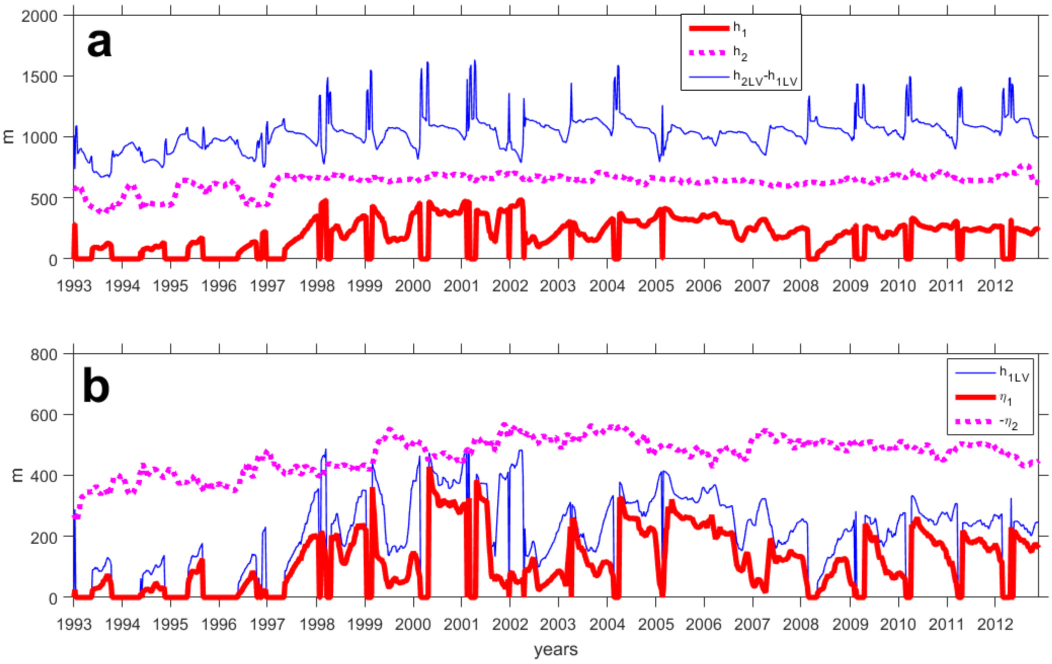

Fig. 6. a - time evolution of the mean layer thicknesses (m) outside the LV: layer 1 (h_1, thick solid red line) and layer 2 (h_2, thick dotted magenta line); time evolution of the LV core thickness (m), - separation between upper and lower interfaces of layer 2 at the LV center (h_{2LV}, thin solid blue line). b - time evolution thickness (m) of layer 1 in the LV center (h_{1LV}, thin solid blue line), and elevation of isopycnals over the LV (m): thick solid red line is η_1, thick dotted magenta line is $|\eta_2|$.

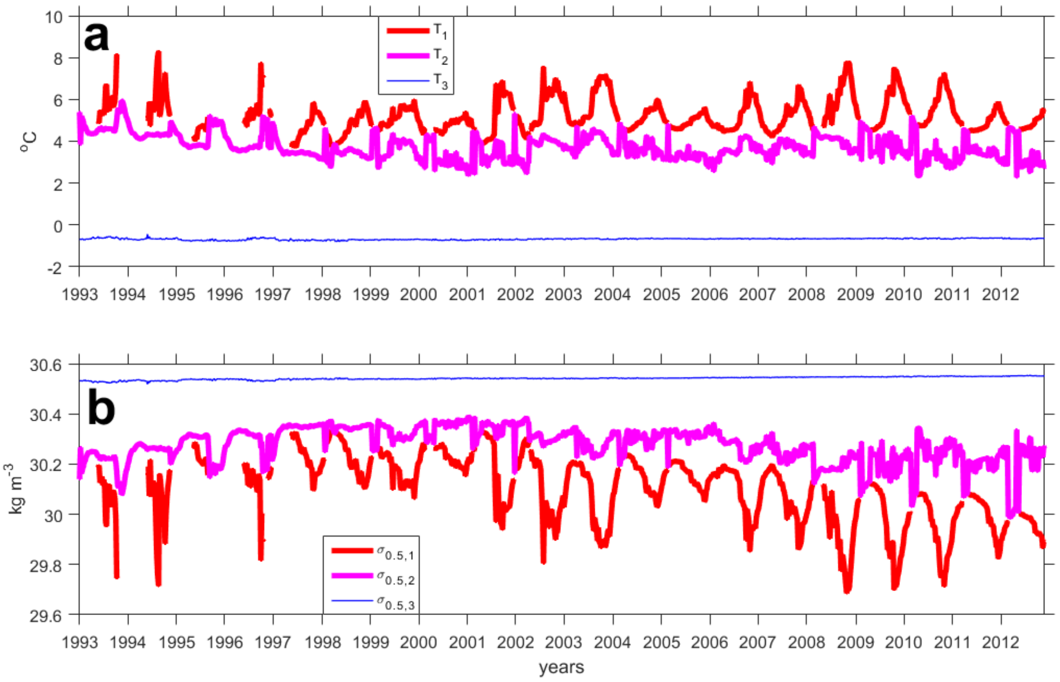

Fig. 7. a- time evolution of layer-mean temperature (°C), b - time evolution of layer-mean density $\sigma_{0.5}$ (kg m^{-3}) in the LV. Red line represents layer 1, magenta line - layer 2; blue line – layer 3.

Figure 8 shows LV radii, velocities and vorticities. The layer-mean radii (Fig. 8a) of the LV in layers 1 and 3 are somewhat larger than in layer 2: the ratios R_2 / R_1 and R_2 / R_3 are on average 0.98 and 0.93, respectively. The ratio of semi-minor to semi-major axes at all depths is on average 0.82 and decreases below 0.70 only for 10% of the time. These results will be taken as justification for using a simple model of a circular columnar LV (see also Fig. 3) in the analysis that follows.

The maximum azimuthal velocity (V_{az}) in layer 1 (V_{az_1}) on average reaches 90% of that in layer 2 (V_{az_2}), while in layer 3 V_{az_3} is about 30% of V_{az_2} (Fig. 8b). Given the small variations of the LV radii with depth, the relative vorticity varies with depth accordingly (ω, Fig. 8c). In idealized 2-layer vortex models, a co-rotating deep flow of 5-10% is already sufficient for stabilizing a vortex (Dewar and Killworth, 1995). Further (Section 3.4) we will show that in a 3-layer QG-model the LV is a subject of a weak vortex instability, while in the primitive equations model with external forcing (Section 3.6) development of perturbations in the LV is restricted to the vortex skirt.

Fig. 8. (a)- time evolution of layer-mean LV radius (km). (b) - time evolution of maximum azimuthal velocity (cm s^{-1}). (c) - time evolution of the mean relative vorticity within the circle $r \le R_j / 2$ around the LV center (s^{-1}). Red line represents layer 1, magenta line - layer 2; blue line – layer 3.

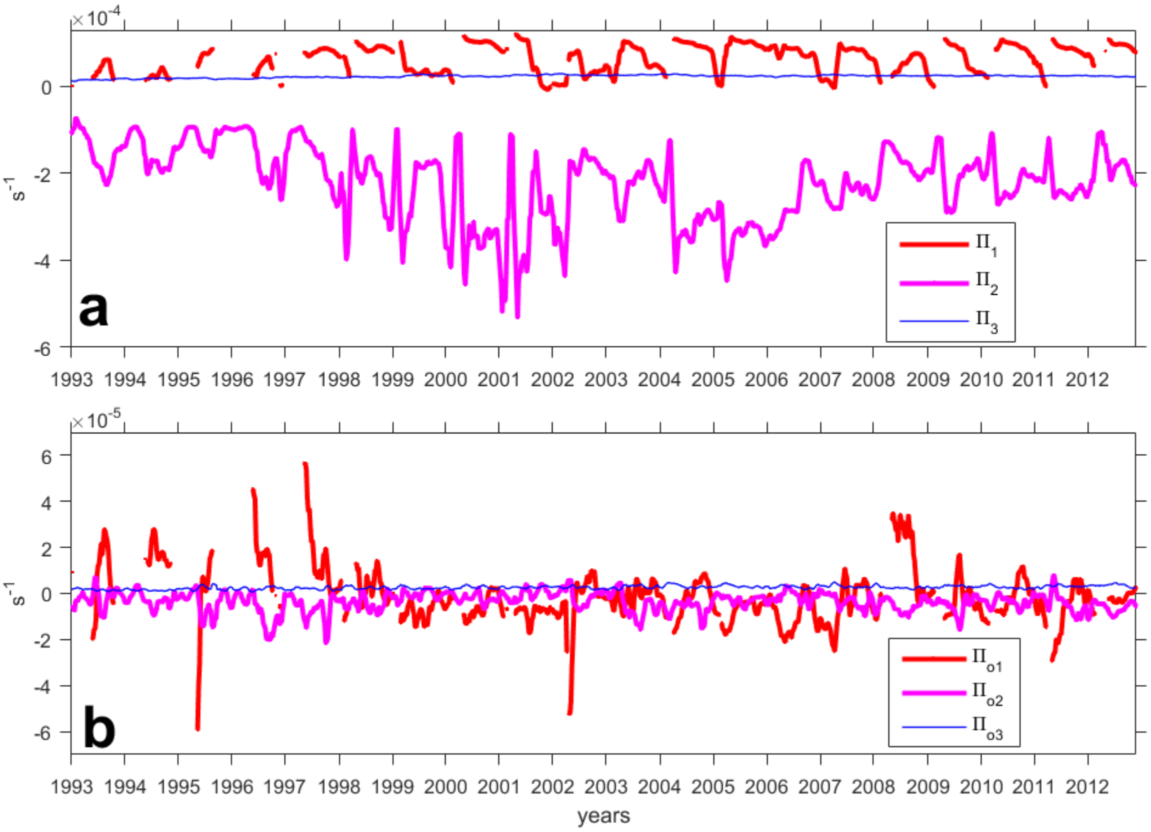

Fig. 9. (a) - time evolution of the layer-mean QG PV (Eq. (1), s^{-1}) in the LV ($r \le R_j$, j =1,2,3 is the layer number). (b) - time evolution of the layer-mean QG PV (s^{-1}) around the LV ($R_j \le r \le 2R_j$). Red line represents layer 1, magenta line - layer 2; blue line – layer 3. Note that y-scale of panel (a) is in 10^{-4} s^{-1}, while of panel (b) is in 10^{-5} s^{-1}.

QG PV for layers 1-3 is estimated as:

$$\begin{cases} \Pi_1 = \omega_1 + f\,\eta_1/h_1 \\ \Pi_2 = \omega_2 - f\,\eta_1/h_2 + f\,\eta_2/h_2 \, . \\ \Pi_3 = \omega_3 - f\,\eta_2/h_3 \end{cases} \qquad (1)$$

Here h_j is the thickness, ω_j is the relative vorticity and η_j is isopycnal deflection in the LV from their mean positions in the surrounding ocean, for layers $j = 1, 2, 3$. Π_2 is negative in the LV core, while above and below $\Pi_{1,3}$ are positive (Fig. 9a). Π_2 outside the LV core ($R \le r \le 2R$) is also negative on average (Fig. 9b), but its absolute value is more than an order of magnitude smaller than $|\Pi_2|$ in the core ($r < R$). The positive PV poles above and below the LV core are formed by squeezing of isopycnals. This suggests that the LV represents a vertically-shielded S-vortex structure (Morel and McWillams, 1997). As the LV is weakly horizontally shielded, its interactions with the mesoscale structures around is expected to be stronger than for an unshielded vortex (Carton 1992; Carton et al., 2002).

3.3. Identification of typical LV PV structures

Figures 6-9 reveal that the overall LV structure remains quite stable in time, except for short periods of deep winter convection, penetrating the LV core. Time-mean parameters of the LV are presented in Table 1. At the same time, a notable time variability of LV parameters exists on seasonal and shorter time scales. In this section we investigate whether much of this variability falls within a smaller subset of typical configurations of the vortex. Typical configurations were identified using K-means cluster analysis performed in the (Π_1, Π_2) parameter space. This parameter space was chosen since layer PVs have a direct influence on vortex stability and since Π_1 and Π_2 show the strongest variations in time (see Section 3.2).

The spread of the LV PV configurations in the $\left(\Pi_1, \Pi_2\right)$ space is shown in Figure 10. The density distribution of the data-points (Fig. 10) shows concentration around 4 distinct centers, marked at the plot as A, B, C and D. Objective selection criteria, like Partition Index and Separation Index decrease slower as the number of clusters exceeds 5, while the Xie and Beni's Index becomes leveled at number of clusters over 3. For example, the Partition Index (the ratio of the sum of compactness to separation distance between the clusters) decreases by 2.9, 2.3, 2.1, 0.2, with an increase of the number of clusters from 2 to 3, from 3 to 4, from 4 to 5 and from 5 to 6, respectively. Therefore, 5 clusters were selected as the optimum number. In the cluster analysis, distances along each of the axes in the $\left(\Pi_1, \Pi_2\right)$ space were normalized by the corresponding ranges of PV values. After such normalization, PV points that lie within a non-dimensional distance of 0.3 from the center of a given cluster were used to estimate the characteristic properties of that cluster (Fig. 10). This avoids transitional states. In total, the four main clusters (A, B, C and D, listed in Table 2) cover over 60% of the model run duration (470 out of 784 model outputs). The mean vertical distribution of isopycnals for each of the clusters are shown in Figure 11. The results are discussed in detail below.

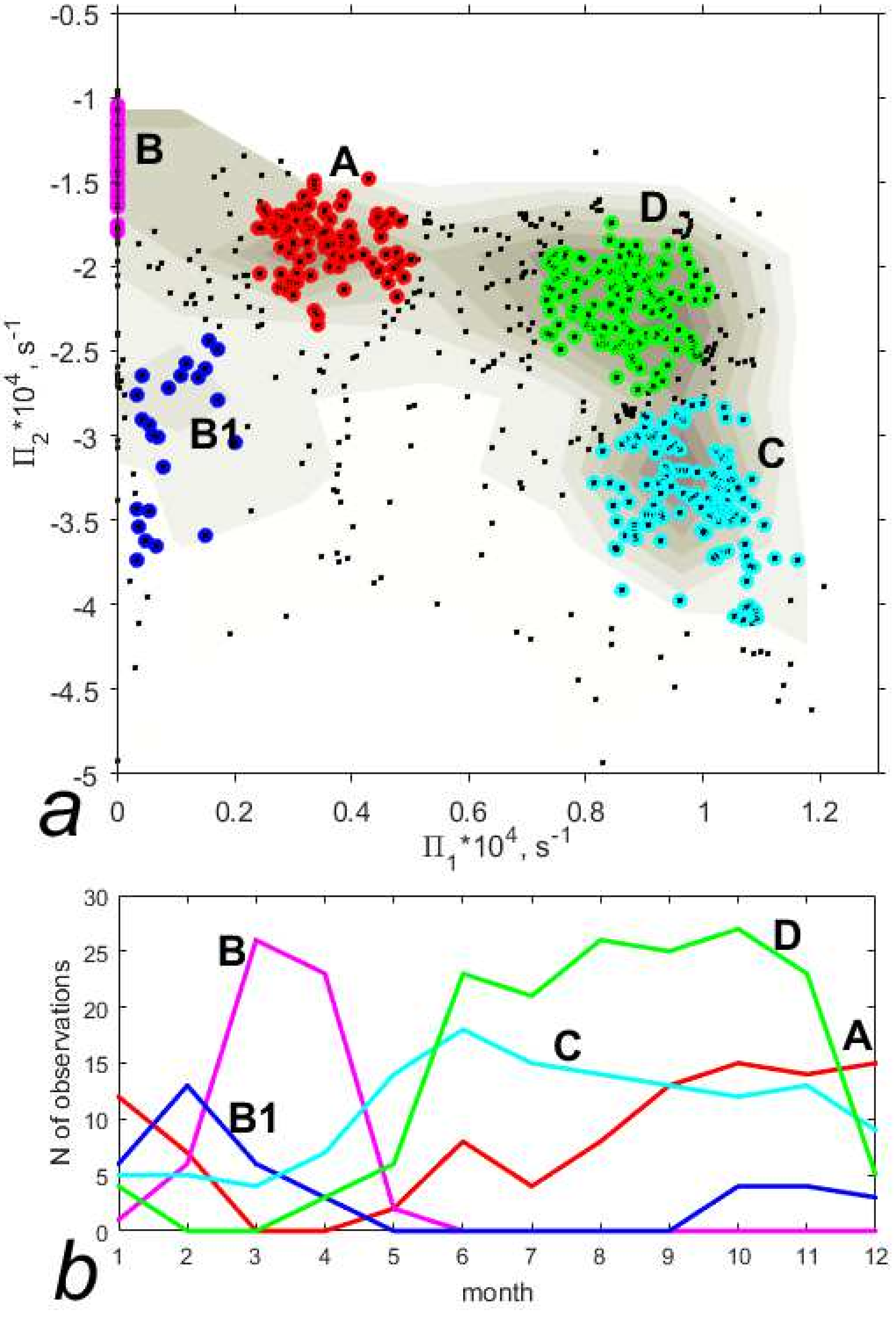

Fig. 10 – The state of the LV in (Π_1, Π_2) space (10^{-4} s^{-1}) and the results of K-mean cluster analysis. (a) Black dots show data points and grey shading indicate their concentration (darker shading indicates higher density). The thicker red, magenta, blue, cyan and green dots represent the (Π_1, Π_2) points identified as belonging to clusters A, B, B1, C, and D, respectively. (b) Number of observations of different states as a function of season over the period of simulations in MIT GCM.

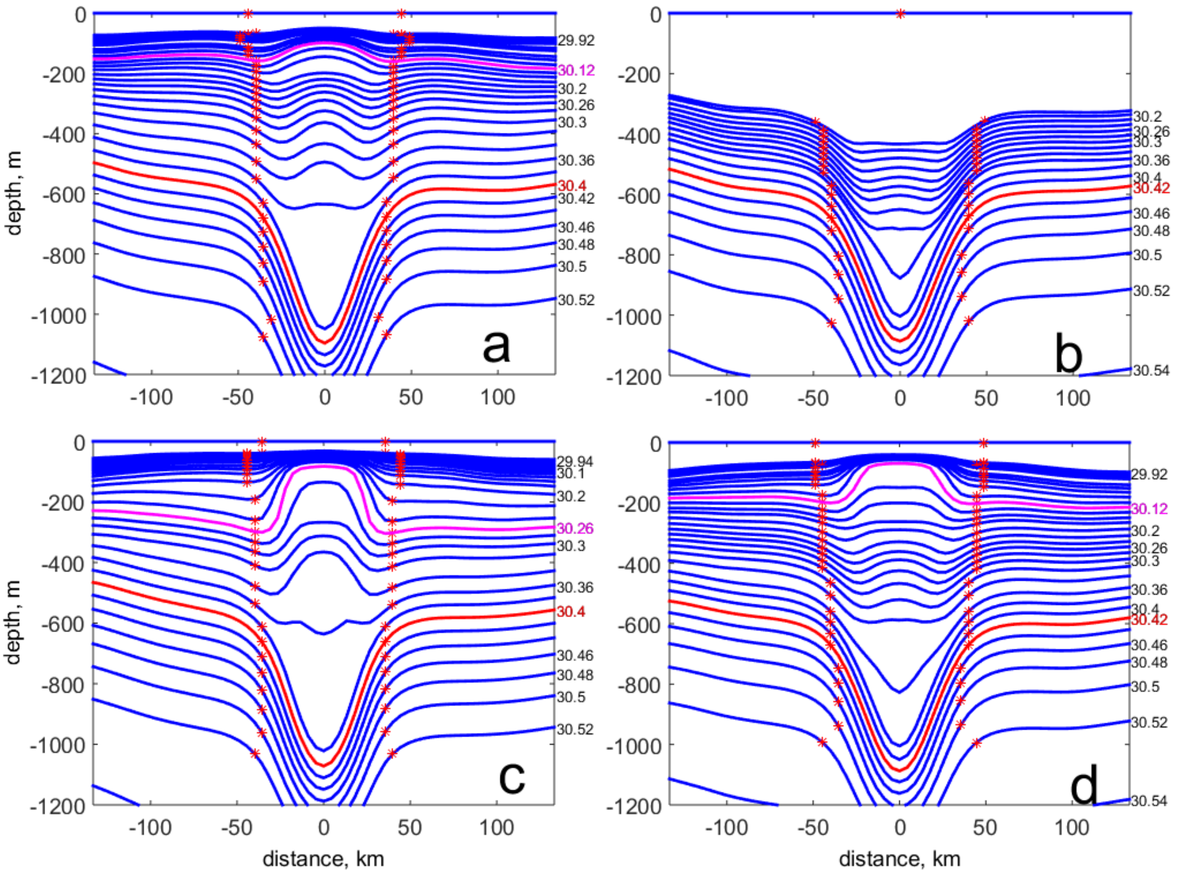

Fig. 11. Mean isopycnal depths (blue lines) across the LV for the four main clusters in Fig. 10. (a) - configuration A, which is the most typical for autumn and early winter, (b) - configuration B, occurring in late winter or early spring, (c) - configuration C, the most typical for late spring, (d) - configuration D, the most typical for summer. Red stars mark the LV limits. Magenta and red lines represent isopycnals, marking the upper and the lower boundaries of the LV core, respectively.

Configuration A (Fig. 10b, 11a) is characterized by small deflections of isopycnals above the LV core (η_1) compared to the mean thickness of layer 1 (h_1), and a comparatively large thickness of layer 2 (h_2). The frequency of such a configuration grows from summer to autumn, slightly decreases in winter and is very rare in spring. In late autumn and winter the upper mixed layer deepens due to convection, gradually eroding the upper boundary of the LV.

Configuration B (Fig. 10b, 11b) is a result of deep convective mixing during the cold season, when the upper layer disappears and a 2-layer approximation of the LV becomes valid: h_1 =0 and η_1 =0; h_2 is anomalously large. This configuration occurs only in early spring. A similar configuration is B1 (not shown in Fig. 11), for which the upper layer exists but the limiting isopycnal over the LV lies much below 200 m, the depth of the upper mixed layer. Configuration B1 is episodically observed from late autumn to early spring, being the most frequent in winter.

Configuration C (Figs. 10b, 11c) is characterized by anomalously large η_1 compared to h_1 , while h_2 is small. This configuration can be observed during any season, but it is most frequent in late spring and early summer, i.e. during the restoration of the seasonal pycnocline. Its frequency decreases through summer and autumn and reaches its minimum in winter.

Configuration D (Figs. 10b, 11d) is intermediate between A and C. This most frequent configuration is the most often observed in summer.

For the study period from 1998 to 2012, from 470 points, used for obtaining the characteristic parameters of each of the configurations (see above), there are 98 points characterized by A-cluster (around 21%), 79 points – by B and B1-clusters (around 17%), 139 points – by C-cluster (around 29%) and 155 points – by D-cluster (around 33%). The rest of the points, not used for construction of the panels of Fig 11, mostly belong to either cluster D or to cluster A. The key vortex parameters for each of the four clusters are listed in Table 2.

Although the sequence A-B(B1)-C-D largely follows the seasonal cycle, interannual variations in the upper ocean stratification under varying atmospheric forcing result in some configurations having overlapping maxima (Fig. 10b). Thus, we may observe configurations A, C or D during summer. During mild and calm winters configurations B (and B1) may not develop (Fig. 9a).

Table 1. Time-mean statistics of dynamic parameters of the LV.

Parameter	Layer 1/interface 1	Layer 2/interface 2	Layer 3/bottom
Interface depth (z , m)	250	655	3000
Layer thickness (h , m)	250	405	2345
Interface deflection at the LV center (η , m)	135	500	0

R, km	30.5	30.0	32.0
V_{az}, cm s^{-1}	-34	-37	-11
ω, s^{-1}	$-1.13\ 10^{-5}$	$-1.32\ 10^{-5}$	$-0.38\ 10^{-5}$
$\lvert\omega_{1,3}\rvert \le \lvert\omega_2\rvert$, %	97%	-	100%
Π *10^{-4}, s^{-1}	0.75	-2.35	0.25
$\overline{\Pi}$ ±std	4.6±1.9	-13.2±5.6	1.4±0.1
$\sigma_{0.5}$ (500m), kg m^{-3}	30.11	30.29	30.54

Table 2. Statistics of dynamic parameters of the LV for each of the clusters (Figs. 10-12).

Parameter	Layer 1/interface 1	Layer 2/interface 2	Layer 3/bottom
configuration A, 21%,			
h ±std (m),	190±65	475±65	2345
η ±std (m)	70±30	-510±25	
R ±std (km)	31±3	30±2	32±2
$\sigma_{0.5}$ ±std (kg/m^3)	30.00±0.12	30.27±0.05	30.54±0.00
Π ±std (10^{-4} s^{-1})	0.36±0.05	-1.85±0.14	0.26±0.01
$\overline{\Pi}$ ±std	2.0±0.7	-10.5±2.0	1.5±0.1
configuration B, 17%,			
h ±std (m),		660±30	2340
η ±std (m)		-490±30	
R ±std (km)		31±2	33±3
$\sigma_{0.5}$ ±std (kg/m^3)		30.15±0.11	30.55±0.00
Π ±std (10^{-4} s^{-1})		-1.33±0.14	0.25±0.01
$\overline{\Pi}$ ±std		-6.4±0.6	1.4±0.1
configuration C, 29%,			
h ±std (m),	340±50	310±35	2350
η ±std (m)	270±50	-485±35	
R ±std (km)	29±2	28±1	31±2
$\sigma_{0.5}$ ±std (kg/m^3)	30.18±0.06	30.33±0.03	30.54±0.00
Π ±std (10^{-4} s^{-1})			

$\overline{\Pi}$ ±std	0.98±0.05 5.6±0.5	-3.37±0.22 -19.7±2.7	0.27±0.01 1.4±0.1
configuration D, 33%,			
h ±std (m),	220±50	425±50	2355
η ±std (m)	160±40	-485±40	
R ±std (km)	31±3	30±1	32±2
$\sigma_{0.5}$ ±std (kg/m^3)	30.01±0.14	30.25±0.05	30.55±0.00
Π ±std (10^{-4} s^{-1})	0.86±0.05	-2.22±0.16	0.24±0.01
$\overline{\Pi}$ ±std	4.8±0.54	-12.7±1.8	1.4±0.1

3.4 Instability analysis in a QG model

The findings in sections 3.2 and 3.3 suggest that during the whole period of observations the sign of PV in the LV core is opposite to the signs of PV in the layers above and below. Thus, the necessary integral condition for vortex instability is satisfied (Sokolovskiy, 1997b; Cushman-Roisin and Beckers, 2011). The range of the vortex Rossby numbers suggests that baroclinic or hybrid types of instability can be expected (Ripa, 1992). For the LV the second derivative of azimuthal velocity in radial direction exceeds variation of Coriolis parameter with latitude, and the necessary condition for barotropic instability is also satisfied (Cushman-Roisin and Beckers, 2011). The possible role of baroclinic, barotropic or mixed instability will be the focus of following sections. We start by studying the stability properties of the LV in a two and three layer QG models.

For a 2/3-layer QG model of the LV, the LV is approximated as stacked cylinders (see Figs. 8-9 and Tables 1-2), with PV anomalies constant in each of the layers (Eq. A6 in Appendix 1). The non-dimensional vortex PV anomalies in each of the layers, used in the QG model, are computed as:

$$\begin{cases} \overline{\Pi}_1 = \overline{\omega}_1 + \overline{\eta}_1/\overline{h}_1 \\ \overline{\Pi}_2 = \overline{\omega}_2 - \overline{\eta}_1/\overline{h}_2 + \overline{\eta}_2/\overline{h}_2 \\ \overline{\Pi}_3 = \overline{\omega}_3 - \overline{\eta}_2/\overline{h}_3 \end{cases}, \qquad (2)$$

where $\overline{\omega}_j = \omega_j / \left(\frac{V}{R}\right)$, $\overline{\eta}_j = \eta_j / (Ro \cdot H)$, $\overline{h}_j = h_j / H$ ($j = 1,2,3$), H is water depth and Ro is the Rossby number. The mean LV parameters in layer 2 (Table 1) were taken as the reference scales. This gives V =37 cm s^{-1}, R =30 km (see Table 1), H =3000 m and f = 1.36 10^{-4} s^{-1}. Hence, the relative vorticity normalization scale is V/R = 1.23 10^{-5} s^{-1} and the Rossby number is $Ro = V/(R\ f)$=0.09. Averaging N^2 over the LV core thickness (1000-1200 m, Fig. 10) and over the full H (10^{-6} s^{-2} and 10^{-7} s^{-2}, respectively), the vortex Burgers number $Bu = \dfrac{N^2H^2}{f^2R^2}$ ~0.05-0.10. The ratio of Ro/Bu ~1 is relatively high, but we may still expect the QG approximation to capture the major features of the LV dynamics (Boss et al., 1996). F_1=3.2 and F_2 = 2.9.

For the mean dimensional characteristics of the LV (Table 1), and with the scaling parameters as above, the following set of dimensionless parameters is taken for numerical experiments:

$\overline{R}_1$ =1.033, $\overline{R}_2$ =1.000, $\overline{R}_3$ =1.067,

$\overline{h}_1$ =0.0833, $\overline{h}_2$ =0.1383, $\overline{h}_3$ =0.7784, (3)

$\overline{\Pi}_1$ =4.6, $\overline{\Pi}_2$ = -13.2, $\overline{\Pi}_3$ =1.4,

We first examine the stability of the various clusters for the linearized problem of small perturbation amplitudes. The analytic solution, which can be framed in terms of an eigenvalue problem for a set azimuthal modes m, is presented in Appendix A. It allows us to identify, for each mode m, stable and unstable domains that are separated by neutral surfaces in the space of PV (Π_1, Π_2, Π_3). Figure 12 shows sections of these hyper-surfaces by a (Π_1, Π_2) plane at a fixed value of Π_3=0.25 10^{-4} s^{-1} (see Table 2) for configurations A, C and D, and by a (Π_2, Π_3) plane at a fixed value of Π_1 =0 s^{-1} for configuration B (when no upper layer exists). Calculations of a set of instability modes for each of the clusters A-D are done for the sets of dynamic parameters presented in Tables 1-2. The area of instability for an azimuthal mode m lie to the right of the neutral stability curve, marked by the corresponding mode number (Fig. 12 a, c, d) or in-between the two neutral stability curves of the same mode number (Fig. 12 b). For each of the cluster configurations (Figs. 10-12), the following azimuthal modes are unstable: configuration A – m =2-3, configuration B – all m, configuration C – m =2-6 and configuration D – m =2-4.

The growth rate for an azimuthal mode m is defined by the imaginary part of the complex frequency $m\ \delta$ (Appendix A). For the mean vortex parameters (Table 1, the thick grey circle in

Fig. 12d) we get linear growth rates $2|Im\,\delta_{m=2}| = 0.0839$, $3|Im\,\delta_{m=3}| = 0.5364$, $4|Im\,\delta_{m=4}| = 0.3316$, i.e. $3|Im\,\delta_{m=3}|>4|Im\,\delta_{m=4}|>2|Im\,\delta_{m=2}|$. Therefore, theoretically, the 3rd and the 4th azimuthal modes are growing much faster than the 2nd mode. The 1st azimuthal mode has zero growth rate. These results are applicable for the most frequent configuration D. The numerical experiments for three other configurations (A, B and C, Table 2) indicate that, the 3rd azimuthal mode dominate the instability also in configurations A and B, and the 5th azimuthal mode – in configuration C. In all the configurations, the most unstable perturbations have a e-folding time scale of order of 60 days.

In a 2-layer model, all modes develop slower, but the lower modes finally are more efficient in decay of the vortex (Table 3).

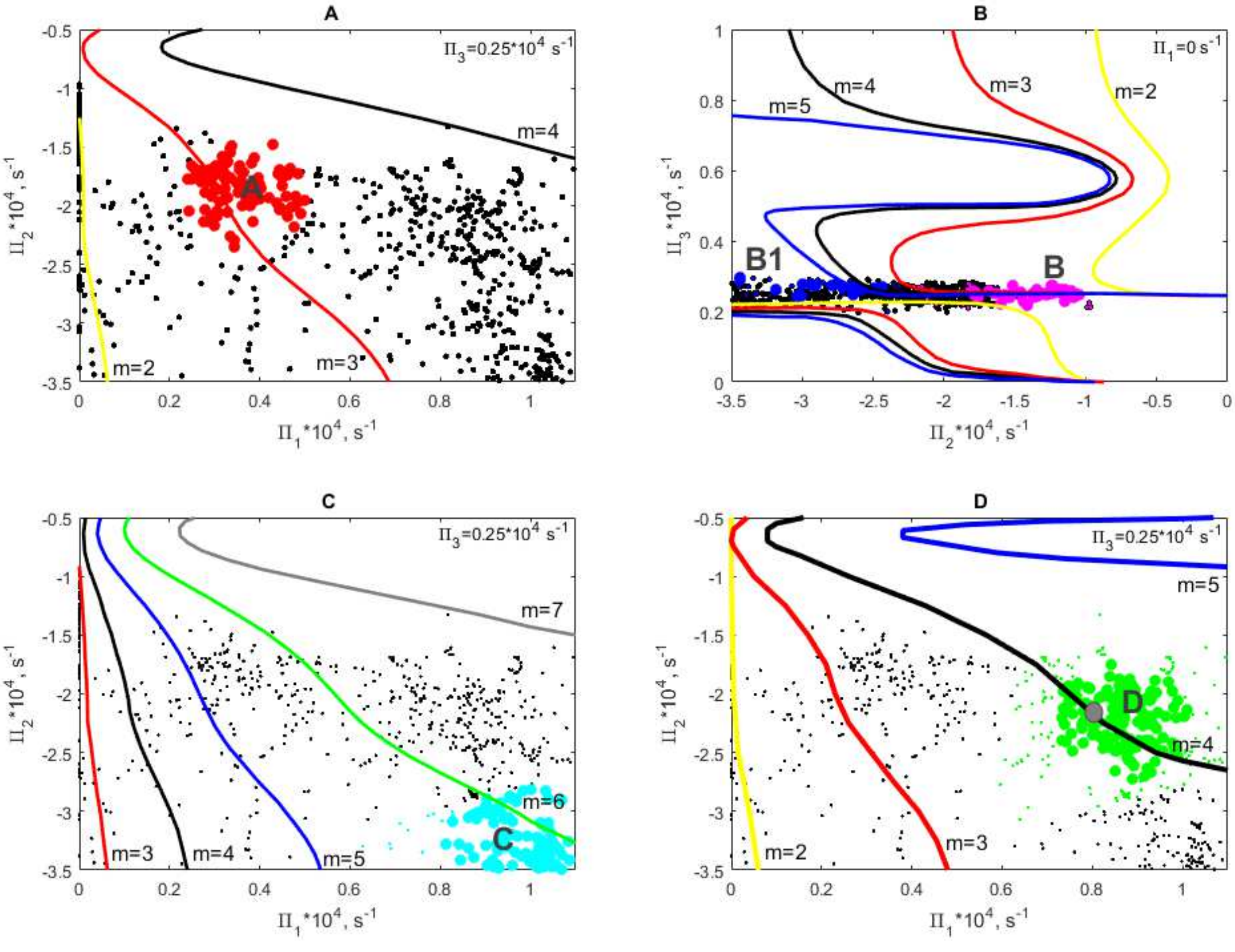

Fig. 12. Same as in Fig. 10 but now with the addition of neutral stability curves based on QG calculations for each of cluster configurations. Colour circles at each of the plates mark the central set of the corresponding cluster (as in Fig. 10), the dots of the same colour – the rest of the points, belonging to the corresponding cluster. The yellow, red, black and blue are lines of

neutral stability curves for azimuthal modes $m=2$, $m=3$, $m=4$ and $m=5$, respectively. (a) the LV PV anomalies (10^{-4} s^{-1}) in (Π_1, Π_2) parameter space for configuration A; (b) the LV PV anomalies (10^{-4} s^{-1}) in (Π_2, Π_3) parameter space for configuration B; (c) the LV PV anomalies (10^{-4} s^{-1}) in (Π_1, Π_2) parameter space for configuration C; (d) the LV PV anomalies (10^{-4} s^{-1}) in (Π_1, Π_2) parameter space for configuration D. The unstable domains of the azimuthal modes are located to the right of the lines with the corresponding labels (in-between the lines of the same mode for (b)). The gray circle in plate (d) marks the PV anomalies of the reference vortex, used for the QG non-linear simulations.

In the numerical non-linear QG study below we will present the non-linear development of instability for azimuthal modes $m=2$, 3 and 4 for the most typical 3-layer configuration of the LV characteristics (Table 1) and for the 2-layer configuration B (Table 2). Under the assumption of a piecewise-constant potential vorticity distribution, simulating the vortex patch, the so-called Contour Dynamic Method (Zabusky et al, 1979) can be applied to a three-layer quasi-geostrophic model (Sokolovskiy 1991, Sokolovskiy and Verron, 2014). The horizontal along-contour resolution in the Lagrangian model has 240 nodes for a circle contour of a unit radius. The number of points increase proportional to the growth of a contour length to keep the original along-contour resolution. In the following experiments (Figs. 13-18) the vortex is immersed in a motionless fluid over a flat bottom. An experiment with a background mean flow and variable bottom topography is presented in Appendix B.

The non-linear QG model is formulated for each of the layers j as:

$$\frac{d\overline{\Pi}_{\mathrm{j}}}{dt} = 0, \tag{4}$$

where the layer PVs are defined as in Eq. (2) and $\frac{d}{dt}$ is the full derivative.

Two sets of runs were made, one with small-amplitude initial perturbations, $\varepsilon_j = 0.02$ and another with larger perturbations, $\varepsilon_j = 0.2$ (see Appendix A, Eq. A.8), In the first case the amplitude of the perturbation displacements of the vortex boundary are small compared to the mean dynamic radius of the LV, in the second case they are comparable to the mean dynamic radius.

For small-amplitude initial perturbations (Figs. 13-15) the predictions of the linearized theory are largely confirmed. In the 3-layer model, for a perturbation with $m = 2$, the main core undergoes a strong elliptical deformation, but keeps its integrity for months (Fig. 13). Two secondary eddies eventually separate from the main core after 6-7 months, but a fairly significant volume of the vortex patch remains in the central part at the end of the 8-months simulation period (Table 3). This demonstrates a significant stability of the vortex to such perturbations: the percentage of volume left in the vortex core at the end of the 5-month simulation period is the largest of all modes (Table 3). Azimuthal mode 3 develops faster and secondary eddies separate from the main core already within 4-5 months (Fig. 14). Mode 4 instability develops nearly as fast, especially in the top layer (Fig. 15). Still, development of secondary eddies of mode 4 is generally limited to the periphery of the vortex, in particular for layers 2 and 3. In these layers the core volume of the main vortex practically does not change after 5-months of development of the instability (Table 3). This suggests a relatively low efficiency of mode 4 in the LV decay for small-amplitude perturbations.

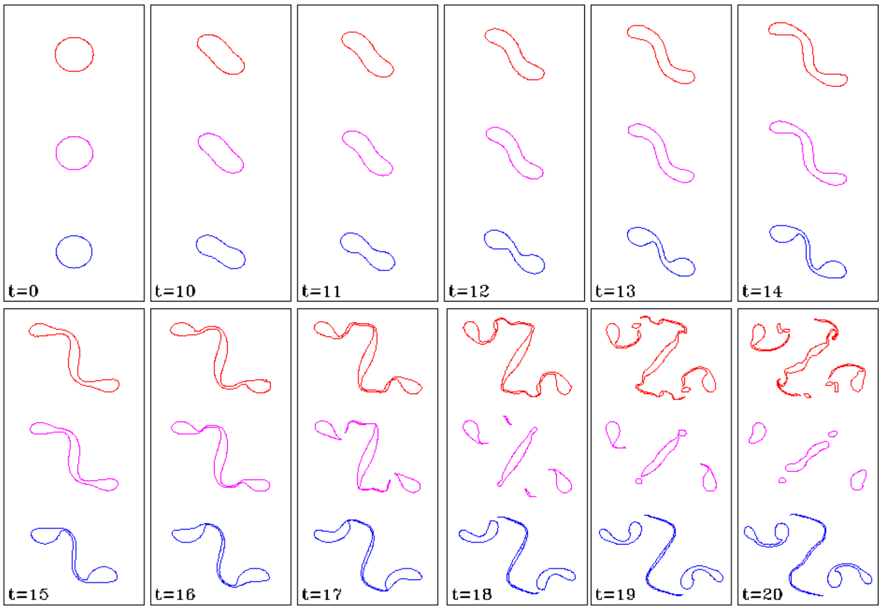

Fig. 13. Evolution of instability in the numerical QG model for small-amplitude ($\varepsilon_j = 0.02,\ j = 1,2,3$) mode-2 ($m = 2$) initial perturbations (see Eq. A.8, Appendix A). The most typical parameter state (Table 1, within configuration D) is used for the model set-up. Each frame shows vortex patches in the upper (red upper contour plots in a plate), middle (magenta middle contour plots in a plate) and lower (blue lower contour plots in a plate) layers as function of non-dimensional time. The dimensionless time unit corresponds to 12 days.

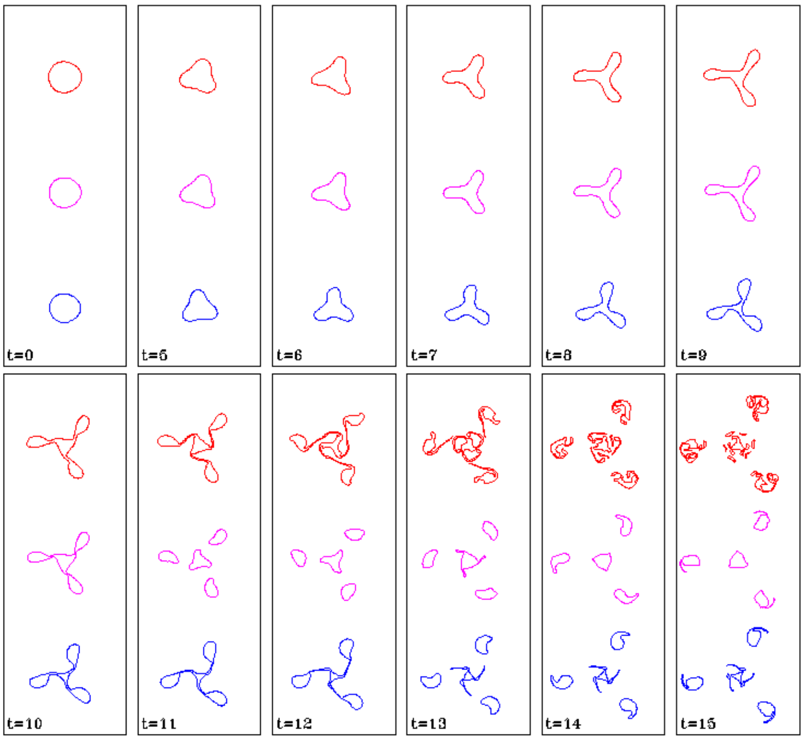

Fig. 14. The same as Fig. 13 but for $m = 3$.

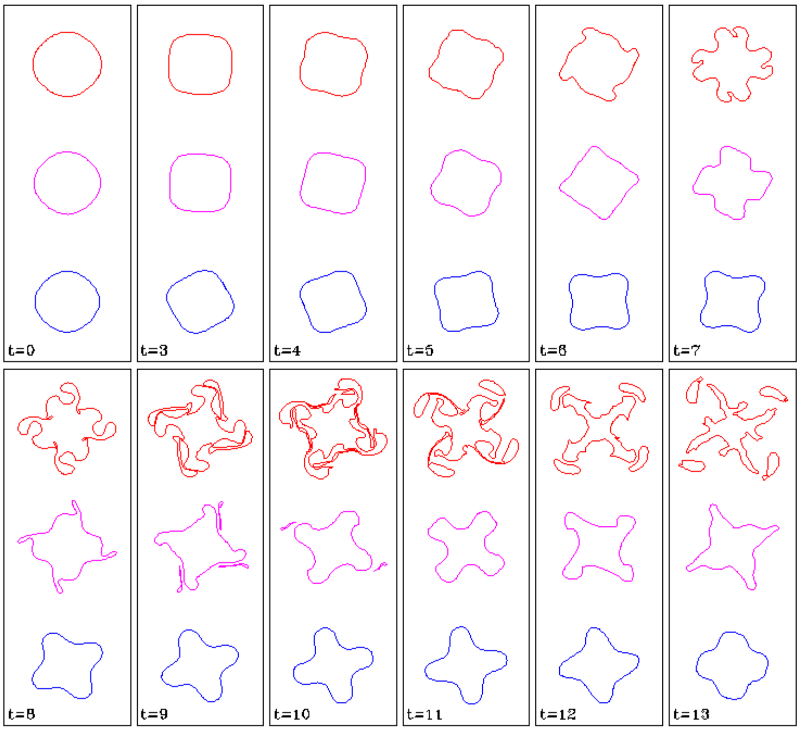

Fig. 15. The same as Fig. 13 but for $m = 4$.

Table 3. A measure of vortex instability: the volume of the central part of the vortex after 5 months for $\varepsilon_j = 0.02$ and for $\varepsilon_j = 0.2$, in percent of its initial volume. In some cases for $\varepsilon_j = 0.02$ the volume ratio at the end of the 5-month period is 100%. For those cases the ratio at the end of the 8-month simulation period is also presented in parentheses.

Perturbation intensity:		$\varepsilon = 0.02$			$\varepsilon = 0.20$		
Azimuthal mode:		*m*=2	*m*=3	*m*=4	*m*=2	*m*=3	*m*=4
3-layer configuration (D)							
Layer number (*j*)	1	100% (37%)	15%	46%	31%	5%	36%
	2	100% (37%)	27%	89%	44%	20%	46%
	3	100% (17%)	16%	99%	0%	6%	15%
2-layer configuration (B)							
Layer number (*j*)	2	100% (59%)	100% (45%)	100% (54%)	71%	51%	52%
	3	100% (36%)	100% (20%)	100% (165)	100%	26%	17%

Increasing the amplitude of the initial perturbations by an order of magnitude leads to rather significant changes in the development of the instabilities (Figs. 16-18). In this case, the linear stability analysis provides less reliable predictions. For all azimuthal modes allowed for the most typical LV vertical structure (2-4), secondary vortex patches are formed within 3-4 months, and after 5 months the main vortex core in the upper and lower layers have decreased significantly in size (Table 3). In the middle layer, the instability with $m = 3$ (Fig. 17) is the most efficient in breaking up the vortex in the 3-layer case (Table 3). In the 2-layer winter configuration B the 2nd mode develops much slower than the 3rd and the 4th ones in the case of finite-amplitude perturbations. The instability with $m = 4$ initially develops nearly as fast as that with $m = 3$ in the LV core (Table 3). Still, for $\varepsilon = 0.20$, further development of the instability modes (not shown) suggests a stronger decrease of the LV volume due to the instability with $m = 3$ at the end of the 8-month period.

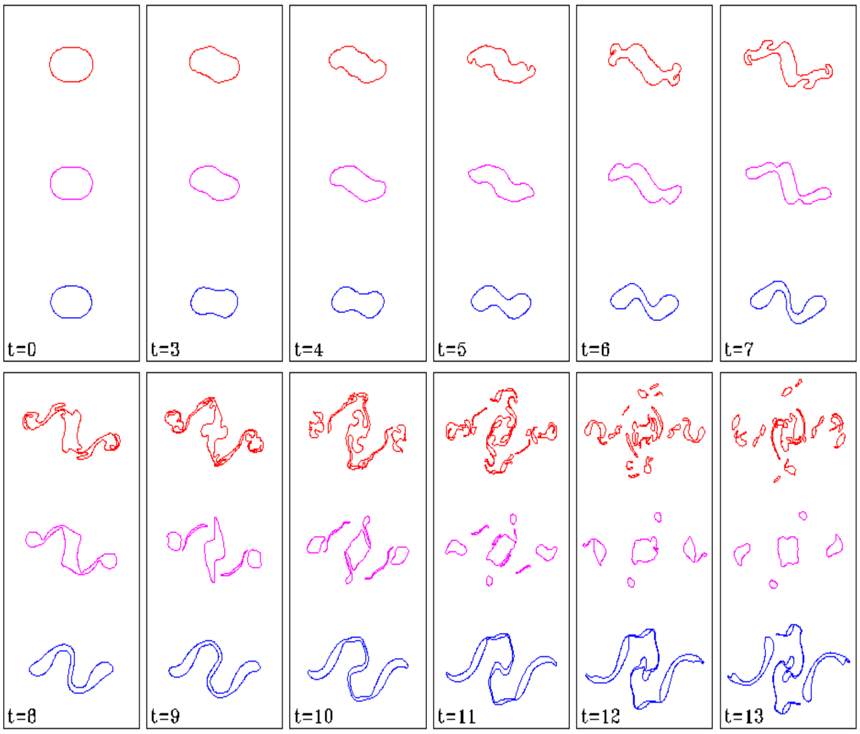

Fig. 16. Evolution of instability in the numerical QG model for finite-amplitude ($\varepsilon_j = 0.2,\ j = 1,2,3$) mode-2 ($m = 2$) initial perturbations (see Eq. A.8, Appendix A). The most typical parameter state (Table 1, within configuration D) is used for the model set-up. Each frame shows vortex patches in the upper (red upper contour plots in a plate), middle (magenta middle contour plots in a plate) and lower (blue lower contour plots in a plate) layers as function of non-dimensional time. The dimensionless time unit corresponds to 12 days.

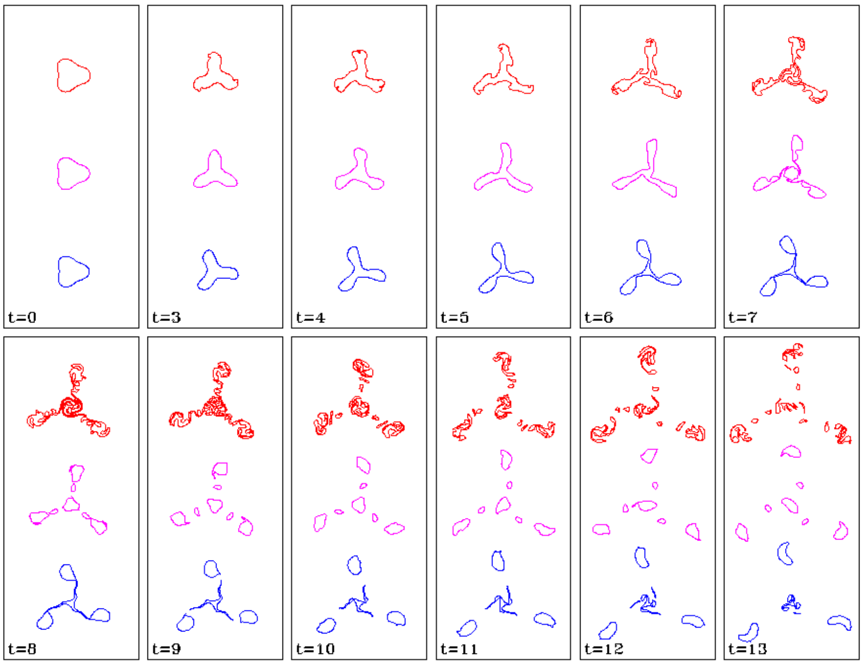

Fig. 17. The same as Fig. 16 but for $m = 3$.

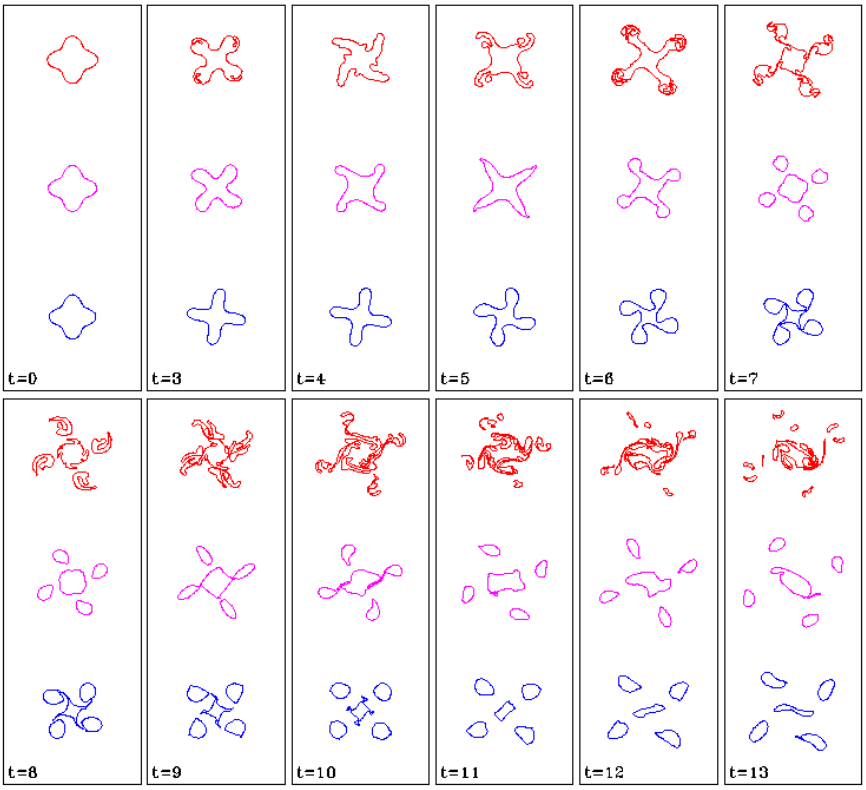

Fig. 18. The same as Fig. 16 but for $m = 4$.

The results of this Section may be summarized as follows. For a realistic set of parameters, both the linear analytical and nonlinear numerical QG models suggest that the LV is weakly unstable. The LV core keeps its integrity at least over 4-5 months, but its volume decreases. For finite-amplitude disturbances, the instability develops somewhat faster and the LV loses more than 50% of its initial volume within the above-mentioned period of time. In the 2-layer case perturbations develop at a noticeably slower rate, which suggests a higher stability of the LV in winter (configuration B). Perturbations with the azimuthal mode 3 appear to be overall more efficient in facilitating vortex break-up than other modes. This distinction is more pronounced for small-amplitude initial disturbances. In many cases the rates of development of 2nd or 4th modes are close to that of the 3rd one. In these cases, other modes than the 3rd one may become dominant in the course of non-linear interactions between the modes in the full complexity of the realistic LV dynamics. For stronger deflection of isopycnals (configuration C, Fig. 10) higher azimuthal modes may start dominating the instability.

3.5 Instability analysis in a QG model with sloping topography

In the previous sections stability of the Lofoten vortex in the 3-layer QG model is done under assumption of the flat bottom and the surrounding fluid at rest. Meanwhile, observations and model results (Sections 1 and 2.1) show that the bottom of Lofoten Basin is gently sloping southwestwards down from 3000 to 3250 m over 250 km, and then sharply rise to 2000-2500 m at the ridge following Jan Mayen Fracture Zone and to 1500-2000 m at the Vorming plato over less than 70 km distance. The Lofoten vortex (Fig. 1) is positioned over the gentle slope in the central part of the basin. In this case the scaling factor of the planetary β-effect, $\frac{\beta}{f} \sim \frac{8.6\cdot 10^{-12}\ m^{-1}s^{-1}}{1.3*10^{-4}s^{-1}} = 0.6\cdot 10^{-7}\ m^{-1}$, is several times less than the topographic β-effect, $\frac{\nabla H}{H} \sim \frac{(3240-3000m)/250km}{3100m} \sim 3.1\cdot 10^{-7}m^{-1}$. Incorporation of planetary or topographic β-effect increases stability to the mean flow (Cushman-Roisin and Beckers, 2011; Hetland, 2017), but for an axisymmetric vortex the stabilization by a gently sloping bottom of the Lofoten Basin is not obvious, as PV now varies along the circular particle path. The cyclonic circulation along the inner part of the Lofoten Basin boundaries (Poulain et al., 1996; Gascard and Mork, 2008) increases horizontal shear gradients at the LV boundary. The current and topography impose perturbations to the vortex, so instability here is generated within the system and is not artificially imposed as in the previous section.

With a barotropic north-easterly mean flow, the so defined “background” state are taken into account by adding new time-independent terms to the right-hand side of equation (A.7):

$$p_{0j}(x,y) = -U_0\, y + V_0\, x - \sum_{i=1}^{8} \sigma_i T_{ij}, \quad i = 1,\ldots,8;\ j = 1,2,3; \qquad (5)$$

where

$$T_{ij} = \begin{cases} \dfrac{r_i}{4} - \dfrac{q_{j2}s_{23}}{s_{13}\gamma_1^2}\left[1-\gamma_1 \mathrm{K}_1(\gamma_1 R_i)\mathrm{I}_0(\gamma_1 r_i)\right] - \dfrac{q_{j3}s_{33}}{s_{13}\gamma_2^2}\left[1-\gamma_2 \mathrm{K}_1(\gamma_2 R_i)\mathrm{I}_0(\gamma_2 r_i)\right], & r_i \le R_i, \\ \dfrac{1+\ln(r_i)^2}{4} - \dfrac{q_{j2}s_{23}}{s_{13}\gamma_1}\mathrm{I}_1(\gamma_1 R_i)\mathrm{K}_0(\gamma_1 r_i) - \dfrac{q_{j2}s_{23}}{s_{13}\gamma_2}\mathrm{I}_1(\gamma_2 R_i)\mathrm{K}_0(\gamma_2 r_i), & r_i \ge R_i, \end{cases} \quad i = 1,\ldots,8;\ j = 1,2,3.$$

Here p_{0j} is an analytically estimated pressure perturbation in each layer j, which is added to the pressure perturbations by the vortex (A.7), to make the total pressure (streamfunction) field. U_0, V_0 are current velocity components at infinity, σ_i is the bottom elevations over 3000 m (negative for a depression) normalized for the area of the circular topographic forms with coordinates of the centers (c_{ix}, c_{iy}), and $r_i = \sqrt{(x-c_{ix})^2 + (y-c_{iy})^2}$; U_0 and V_0 are the scales of the zonal and the meridional components of the mean barotropic flow. Other notations are presented in Appendix A.

As the first step, an effect of a relatively small localized bottom depression on the LV stability (Köhl, 2007) is numerically verified (Appendix B). Although it was previously shown that the LV, most of the time, is not situated over any of the 50-m bottom depressions in the center of the Lofoten Basin (Figs. 1-2), episodically it is observed over one or another depression. Non-linear QG simulations show that, as in Section 3.4, instability filaments are formed 2-3 months after the beginning of the simulations, triggered by interaction of the LV with the topography and the mean flow. Topographically induced deformations of the vortex are especially pronounced in the lower layer (Fig. B1). During 2-3 months, we observe over 50% reduction of the volume of the LV main core in the upper 2 layers, while the LV is totally destroyed within 5 months (Fig. B1). Thus, the decay rate is close to that of the flat-bottom case, when finite-amplitude perturbations are imposed (Section 3.4). Thus, localized bottom depressions and the background current alone may lead to a relatively fast decay of the LV in the QG model.

Another interesting result of Appendix B is that all the filaments and submesoscale eddies, formed as a result of the LV instability, remain inside the Lofoten Basin for at least 6 months of the simulations. This may have implications for mechanisms of maintenance of the observed anomalously thick layer of Atlantic water in the Lofoten Basin (Björk et al., 2001; Søiland and Rossby, 2013).

As the second step, we neglect the effects of relatively small depressions around the mean position of the Lofoten vortex (Fig. 1), but take into account the large-scale effect of the gently sloping bottom topography in the central part of the basin. For this, we approximate the realistic topography of the central part of the Lofoten Basin with 8 circular non-concentric cylinders with radii of 175, 147, 125, 105, 80, 60, 45, 30 km and depths of the plains equal to those of the outer rings of 3000, 3100, 3150, 3200, 3225, 3230, 3235 and 3240 m, respectively (Fig. 19).

Figure 19 presents configurations of the streamlines for the background initial conditions, when the mean flow at infinity is $U_0 = 10$ cm s^{-1} and $V_0 = 4U_0$. Specifically, the bottom elevation between 3000 and 2000m and the background velocity field forms open streamlines, cyclonically skirting the eastern part of the basin, while along its western boundary the strait northwards current is formed (Fig. 19). This simulates the mean upper ocean circulation in the Lofoten Basin (Fig. 1). At this point, we note that in the results below all moving vortex patches remain within the 3000 m circle, and the topography outside the 2000-m contour does not directly affect the LV. We also note that in the southwestern part of the deep Lofoten Basin, a pattern with closed streamlines is formed, separated with a separatrix streamline (the thick black line in Figure 19). This area disappears for higher velocity of the background flow (U_0 > 50 cm s^{-1}, not shown).

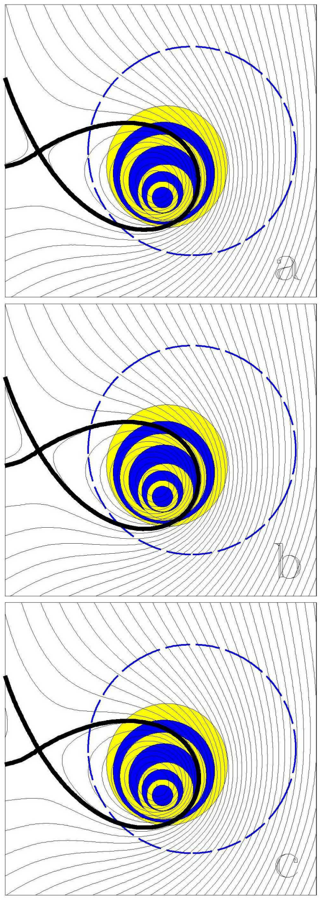

Fig. 19. The initial state of the QG model with varying topography and the mean flow. The topography presents a set of nested non-concentric cylinders with different depths and radii (marked alternatively with yellow and blue, see text for details). The dashed blue contour presents the 2000 m isobath; with radius of 600 km, it marks the boundary of the Lofoten Basin in the model. Gray contours are the streamlines. Black line marks the separatrix, which limits the area, where particles are not advected out of the simulation region by the mean flow.

Numerical experiments for the configuration above (Fig. 19) provide the evolution of the LV in the presence of a gently sloping topography and the background flow of are presented in Figures 20 and 21. As in Appendix B, the initially circular vortex patch is not artificially perturbed, as the background deformation flow field itself generates sufficiently strong non-linear instability perturbations at the vortex boundary.

The evolution of the LV suggests the fundamental role of existence of the separatrix in the mean current field in evolution of the vortex patches in the area. In particular, Figures 20 and 21 differ only by the initial position of the vortex in the area: inside the central area of the closed streamlines of the mean flow: the vortex center initially coincides with the stationary elliptic point (Fig. 20), or the vortex initial position is moved towards the hyperbolic point of the separatrix (Fig. 21). This leads to quite different evolutions of the initially circular vortex patches, as well as to different vortex decay times.

Fig. 20. Simulations of the LV evolution in a QG model, when a barotropic background flow and varying bottom topography is approximated with 8 circular non-concentric cylinders with varying plain-depth and radii, and the northeasterly mean flow is added (see Fig. 19 and text for details). The LV is initially centered at the elliptic point of the mean background velocity field. As before, the LV set-up is presented by its most typical parameter state (Table 1, within configuration D). Each frame shows vortex patches in the upper (red upper contour plots in a plate), middle (magenta middle contour plots in a plate) and lower (blue lower contour plots in a plate) layers as function of non-dimensional time. The unperturbed (initial) position of the separatrix is given for reference. The dimensionless time unit corresponds to 12 days.

Positioned in the central part of the basin (Fig. 20), even 7 months after the beginning of simulations (t=18), the vortex keeps the nearly circular shape. This radically differs from the flat-bottom case with no mean flow (Figs. 14-18), or from the results of Appendix B (Fig. B1).

The separation of the vorticity patches starts only about a 1 year after the beginning of simulations (t=24-30). As in Appendix B, the during the vortex decay topography efficiently traps the vorticity patches, which stay within the loop of the separatrix during all the period of simulations.

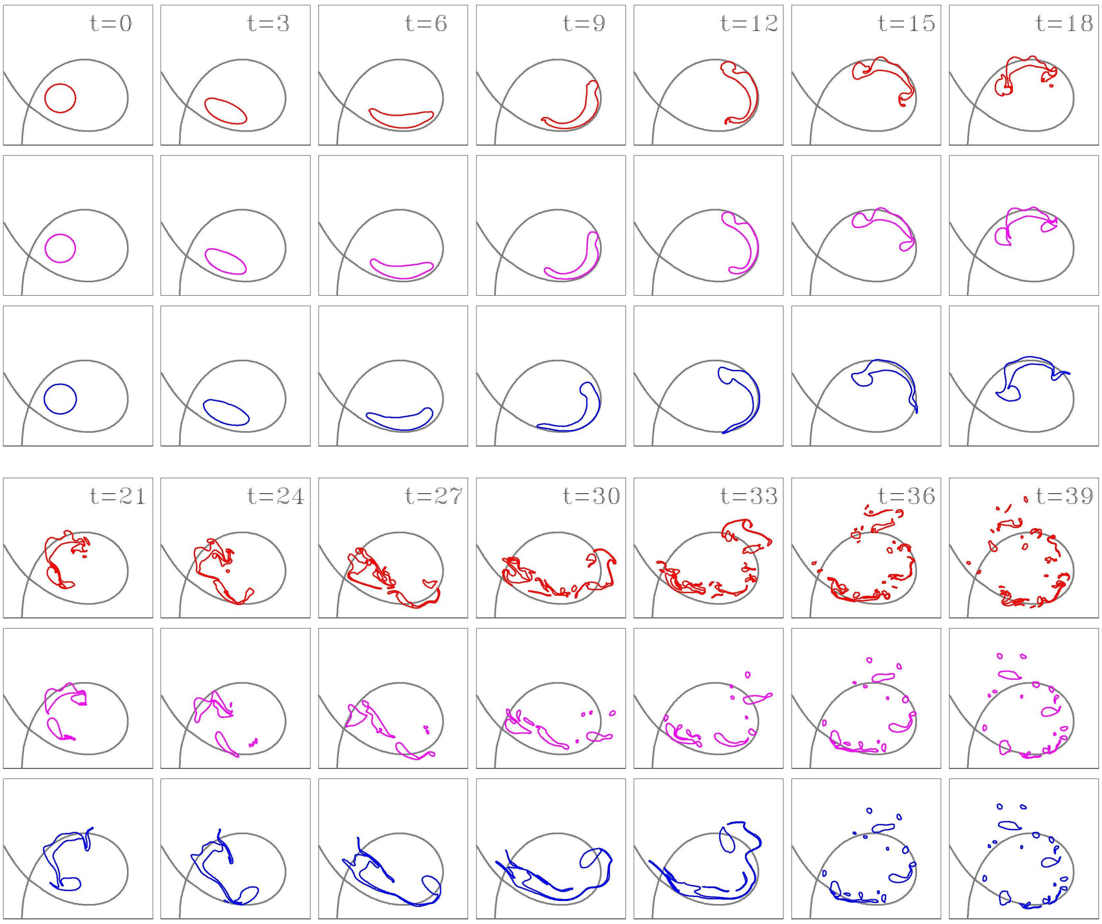

Fig. 21. As in Fig. 20, but the initial position of the LV is shifted southwestwards, towards the hyperbolic point.

Positioning the vortex closer to the hyperbolic point, leads to its much faster decay (Fig. 21). Deformed by the current shear, the vortex becomes strongly elliptic already 1-2 months after the beginning of the simulations. However, it takes 6-8 months ($t = 15 - 21$) before the vortex breaks into separate vorticity patches. At the end of the modelled evolution, a significant fraction of the vorticity patches remain within the region, surrounded by the separatrix.

At the limit, when the vortex is positioned in the hyperbolic point (not shown), the main vorticity patch stretches along the separatrix faster than in Fig. 21. Still, separation of vorticity patches from the main vortex body is observed only 5-7 months after the beginning of the simulations. In this case, nearly all vorticity patches drift out of the central region.

To summarize the results of this paragraph, in a more realistic case of slowly varying topography and with the effect of the mean current, as in of the Lofoten Basin, in the 3-layer QG model demonstrates a significantly slower decay of the vortex, especially when the vortex is entered in the ellyptic point of the background velocity field.

3.6 Disturbances at the LV dynamic boundary in the primitive equation model

Looking for clean evidence of instability in the full-complexity and forced primitive equation simulations is not trivial. Nevertheless, we set out to look for such evidence by diagnosing the relative strength of various PV azimuthal modes near the LV dynamic boundary in the MIT GCM model. The development of the modes will be related to variations in the LV volume and relative vorticity field — to see whether signatures of the QG predictions can be found. We also investigate whether time variability of the LV dynamic parameters are related to the intensity of perturbations at its boundary. The near-surface level (200 m) was chosen since the linear QG model predicts the perturbation amplitudes to be largest in the upper layer. In fact, the primitive equation model shows that azimuthal perturbations in the LV core and in lower levels have 5-10 times smaller magnitudes than those in upper levels.

Could the higher intensity of perturbations at the selected level in MIT GCM partly be attributed to the atmospheric forcing, in fact, the selected level is most of the time below the seasonal pycnocline (Fig. 11) and, thus, not directly affected by the atmosphere (except for the short phases of deep convection – configuration B). Furthermore, the azimuthal perturbations grow by an order of magnitude within the time scales of 3-7 months (Fig. 22). This growth cannot be directly forced by high-frequency atmospheric motions (typical synoptic time scales are of order of a week), but can be attributed to a development of eddy dynamic instability, as observed in the QG model.

The intensities of the perturbations were estimated in three circular rings around the vortex center. The inner ring is positioned at the edge of the LV core, at a distance of $R_{av1} \pm dr$ ($R_{av1} = R_{av}$ is the dynamic radii, where relative vorticity vanishes). The second ring covers the inner skirt of the LV, at $R_{av2} \pm dr$ (R_{av2} is the mean distance from the LV center, where relative vorticity reaches its first local maximum). The third ring covers the outer skirt of the LV, at $R_{av3} \pm dr$ ($R_{av3} = R_{av2} + 2dr$ is in the outer part of the eddy, where the rotation velocity of the vortex decreases to 10% of its maximum value). The distance dr above is selected as the half distance between R_{av1} and R_{av2}. All three rings lie inside the LV, defined as the region of anticyclonic rotation. Within each ring, the PV ($\Pi_E = N^2(f+\omega)/g$) around the LV is averaged in the radial direction to form 3 circular distributions with 10° azimuthal increment. In order to make the results comparable with the QG model estimates (Section 3.4), the circular distributions are transformed into deviations of PV contours from the radial shape ($\varepsilon = \frac{1}{\overline{R}_{av}} \frac{\Pi_E'}{\partial \tilde{\Pi}_E / \partial r}$, where $\tilde{\Pi}_E(r)$ is the mean value of Π_E at a fixed radial distance from the LV center and $\Pi_E' = \Pi_E - \tilde{\Pi}_E$ is the deviation, $\overline{R}_{av}$ is the time mean LV radius). The variability within those circular distributions is further decomposed into sets of azimuthal modes by wavelet techniques using Morlet mother wavelets for the periodic circular domain (Torrence and Compo, 1998).

The wavelet coefficients of relative vorticity peak at the 1st (antisymmetric) azimuthal mode (period = 360°), the 2nd mode (period = 180°), the 3d mode (period = 120°), the 4th mode (period = 90°) and the 5th mode (period = 60°). Assuming a near-sinusoidal shape of the wavelet coefficients for each of the wavelengths of interest, the intensity of each mode is estimated to be 1.4 times the standard deviation of its wavelet coefficients. The intensities of the 1st and the 5th modes are always significantly less than those of modes 2-4 (as also observed in Carton et al., 2014).

Temporal distributions of the intensity of the dominating 2nd to 4th azimuthal modes are presented in Figure 22. The elliptic mode ($m = 2$) is the dominating one, while the energy of higher modes decreases with the mode number. The modes show a considerable amount of co-variability. The median deformations of the circular vortex structure by the 2nd, 3rd and 4th modes represent 12%, 5% and 3% of the dynamic radius at R_{av1}, 16%, 11% and 7% at R_{av2}, and 25%, 20% and 16% at R_{av3}. The presence of the 2nd (elliptic) mode, especially pronounced at R_{av1}, is a result of eccentricity of the LV core which is observed most of the time. The relative intensities of the higher modes increase with the distance from the LV center (R_{av1} to R_{av3}): on average from 50% to 80% for the 3rd mode and from 25% to 65% for the 4th mode—

relative to the intensity of the 2nd mode. In the radial direction the perturbations of the 2nd mode are less correlated than those of the higher modes. For the 2nd mode the correlation coefficients at R_{av1} with the same mode at R_{av2} and R_{av3} are 0.70 and 0.50, respectively, while for the higher modes the same coefficients are 0.90 and 0.75, respectively.

The typical time scale for growth of the perturbation in the MIT GCM model ranges from 3 to 7 months (Fig. 22). This is close to the period of development of baroclinic instability in the idealized QG model of the LV. As the perturbations develop the LV dynamic radius (also shown in Fig. 22) typically stays rather stable. Only after the perturbations reach high amplitudes at R_{av1} and R_{av2} , a notable decrease of the LV radius is seen. Thus, during the most dramatic events in mid-2000 and in mid-2005 the LV radius decreases by about 5 km over 3-4 months. This forms about 15% of the initial LV radius. Assuming a circular shape of the LV, this means about 70% of the LV volume is maintained within the dynamic core. The normalized perturbation intensity in the MIT GCM model (ε in Eq. A.8) reach 0.1-0.2. According to QG model calculations, for such values of ε , the LV instability should decrease the LV volume by at least 50% within 4-5 months (Figs. 15-17 and Table 3). The primitive equation model shows considerably smaller LV volume decay. After separation of a part of the LV skirt, the LV volume (limited by its dynamic radius) is restored in 1-2 months.

Growth of the perturbation intensity typically goes in parallel with a decrease of the LV rotation rate. The magnitude of the relative vorticity of the vortex core (mean relative vorticity within $0.5R$) presents significant negative correlations with the intensity of the perturbations at the LV boundary (Fig. 22a). The correlation coefficients are about -0.5 for all the modes and for each of the 3 selected distances from the LV center. With a 1-year sliding average, the correlation coefficients range from -0.7 to -0.8. Cross-correlations with the azimuthal mode coefficients show that, on average, the absolute values of the core relative vorticity reach a minimum 1-2 weeks after the perturbation disturbances have reached their maximum. The overall rate of the decrease is small. During a period when no merger of LV with other anticyclones is registered (2004-2005), the monthly rate of the decrease of the magnitude of the LV relative vorticity is estimated to 2-3.5%. This suggests a decrease of the LV rotation by 10 to 18% during the 5 months period.

The angular momentum, being a product of the relative vorticity and the squared radius, accounts for relative vorticity distribution in the radial direction. Contrary to the core relative vorticity, the absolute value of the integral angular momentum of the LV core positively correlate with the intensity of perturbations (Fig. 22b). The correlation coefficients are not high, but significant: 0.25 to 0.40. This may stand for a redistribution of the relative vorticity from the LV center to the LV boundary with the growth of the perturbations (Fig. 22a,b).

The intensity of the perturbations in the LV core negatively correlate with the strain around the core (Fig. 22c). The correlation coefficients are significant and range from -0.20 to -0.40, depending on the distance from the LV center and on the azimuthal mode. We consider this to be a sign of the external strain favoring concentration of instability in the vortex skirt, further detached from the LV as isolated filaments.

In Fig. 22d we present potential and kinetic energy anomalies, integrated over the LV volume. The internal volume was taken over the cylinder with the radius 1.6R (where the dynamic radius R is a function of depth and time). The integral kinetic energy is computed as $KE = 0.5\iiint \rho V^2 dx\,dy\,dz$, the integral barotropic potential energy anomaly as $PE_s = 0.5\,g \iint \rho_s\, SLA^2\, dx\,dy$, and the integral baroclinic potential energy anomaly as $PE_i = 0.5\,g \iiint \Delta\rho^2 \Big/ \left|\frac{\partial \bar{\rho}}{\partial z}\right| dx\,dy\,dz$ (Oort et al., 1989). Here V is the azimuthal velocity, g is the gravity acceleration, ρ and ρ_s are water density (subscript s stands for the sea-surface), SLA is the sea-level anomaly over the LV, $\Delta\rho$ is water density anomaly in the LV relative to the background, and $\frac{\partial \bar{\rho}}{\partial z}$ is the background pressure gradient. For computation of anomalies of potential energy in the LV core, the reference state was taken as the mean at distances $[2R{:}\,4R]$ from the LV center. The anomalies relative to the basic state are estimated in each point of the LV core. PE_i is dominating the total energy, while KE is several times less, and PE_s is 4 orders of magnitude less than PE_i. Fig. 22d demonstrates that PE_s and KE have a very immediate reaction on the eddy merger events, while PE_i increase can be delayed after a merger. In most cases merger occurs during the periods of the deep winter convection, and it is difficult to distinguish between the two mechanisms of the LV regeneration. Closer look in Fig.22d suggests that both mechanisms are responsible for the LV re-generation, maintaining the LV integrity against dissipation, previously suggested by Ivanov and Korablev (1995a,b), Köhl (2007), Volkov et al. (2015). In particular, several peaks in PE_s , PE_i and KE occur during summer mergers (2001, 2003, 2009), as well as during winters with no mergers (2000, 2004, 2005, 2010), but no significant peaks are apparent, when none of these events take place. During winter convection events, an increase in PE_s and PE_i is observed, while KE often does not increase (as during convection periods of 2004, 2005 and 2012). This explains why

Volkov et al. (2015), using relative vorticity as a measure of the LV strength, did not find winter convection to have an effect on the LV.

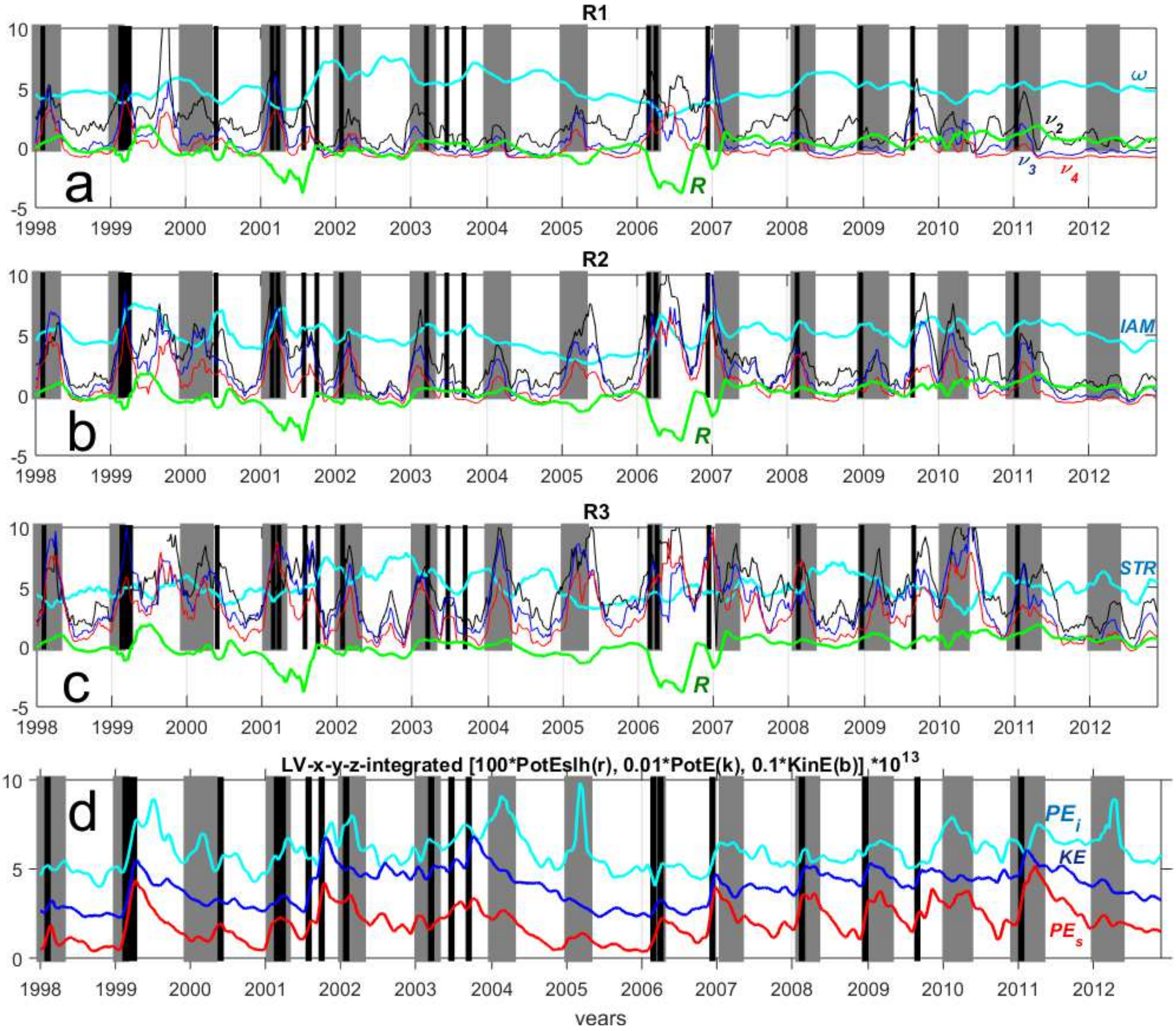

Fig. 22. LV variability in the MIT GCM model at 200 m depth (a-c). In panels (a-c), black, blue and red lines show the variability of perturbations with azimuthal modes 2, 3 and 4, respectively. Panel (a) depicts the normalized perturbations in ring 1 (centered at R_{av}), panel (b) – in ring 2 (centered at $1.5R_{av}$) and panel (c) – in ring 3 (centered at $2R_{av}$). The perturbation intensities are normalized as: $v = (v - v_{4av})/v_{4std}$, where v_{4av} and v_{4std} are time-mean and standard deviation of the perturbation intensity (v) of azimuthal mode 4 in ring 1. Variability of the normalized LV dynamic radius (R_{av}) are shown with green lines. In panels (a-c) LV radius and other parameters below are normalized as: $v = (v - v_{av})/v_{std}$, where v_{av} and v_{std} re time-mean and standard deviation of the corresponding variable. In addition, the following dynamic characteristics of the LV core are shown with cyan lines (for better visibility the lines are centered at y-value 5): panel (a) – normalized absolute value of the relative vorticity of the

LV core (ω, averaged within 0.5 R_{av} from the LV center); panel (b) –normalized absolute value of the integral angular momentum (*IAM*, integrated within the circle R_{av}); panel (c) – normalized strain around the LV core (*STR*, mean in the ring $R_{av} \leq r \leq 2R_{av}$). In panel (d) time variations of barotropic potential energy anomaly (PE_s), baroclinic potential energy anomaly (PE_i) and kinetic energy (*KE*), integrated over the LV core volume. The time series are normalized and vertically displaced for better visibility. The LV mergers with other anticyclones are marked with black solid vertical lines. Shaded areas are winter periods of deep mixing.

In summary, the LV instabilities, developing in the primitive equation model share a number of features of the vortex instability predicted by the non-linear QG model. However, instabilities appear to mostly develop in the LV outer skirt and do not penetrate deep into the LV core (see also Mahdinia et al., 2016). Our interpretation of the observations above is that a frontal geostrophic dynamic model may be more appropriate for re-producing the observed features (Cushman-Roisin, 1986). External strain also favors concentration of instabilities in the skirt and formation of filaments at the LV boundary. Separation of the filaments from the LV removes angular momentum, slowing down its rotation, rather than eddy volume. The migration of the energy of the perturbations towards the skirt prevents from further penetration of the perturbations in the core, and allows the core to persist during longer periods of time.

We also note that the correlation of the relative vorticity of the LV core with the perturbation intensity (0.7 to 0.8) is much larger than correlation of the relative vorticity of the LV core with a number of mergers (0.3). Sliding averages with a 1-year window size are used in both cases.

4. Summary and discussion

In this paper we have presented a study of the vertical structure and stability of the semi-permanent anticyclonic Lofoten vortex (LV). The results are based on eddy-permitting numerical simulations with the MIT GCM and on idealized 3-layer QG model calculations.

The MIT GCM fields demonstrated that the LV is a columnar vortex, extending from the sea-surface to the bottom, with a dynamic radius *R* of about 30 km (Fig. 4, Table 1). The first baroclinic Rossby radius of deformation R_d in the Lofoten Basin is about 7 km (Nurser and

Bacon, 2014; also obtained from the MIT GCM results), so $R \sim 4R_d$. The vertical structure of the LV contains a noticeable baroclinic component. The vortex core is found between 50-200 m and 900-1100 m and is associated with a maximum in azimuthal velocity and relative vorticity as well as a minimum in dynamic radius. The core is characterized by a weaker stratification, giving rise to a pronounced negative PV anomaly with respect to the surrounding ocean conditions.

The vertical structure of the LV varies in time, demonstrating seasonal and intra-seasonal changes. A large part of this variability falls within four-five distinct clusters in the phase space of layer-mean QG PV of layers 1 and 2 (Fig. 10). Each cluster is characterized by a certain configuration of isopycnals, mostly differing by depth of the isopycnals at the top of the vortex core relative to their depths in the surrounding ocean (Fig. 11). The LV states in the PV space are mostly concentrated near the centers of one of these clusters. This means that the transitions between the states are rather rapid. The transitions between the states are formed by variation of the upper ocean stratification over the LV core, which is a function of atmospheric forcing. A 3-layer vertical structure, with the core in the middle layer, is found to be an adequate representation of the vortex most of the time (clusters A, C and D). The 2-layer configuration (clusters B and B1) is observed 17% of time. It occurs during some late winters or early springs, when deep convective mixing erodes the upper ocean stratification over the LV and reaches the LV core.

In-situ observations (Ivanov and Korablev, 1995a,b; Raj et al., 2015) are too few to allow a detail classification of all LV vertical states. Still the observations confirm the existence of at least the two limiting states derived from the MIT GCM: a summer-autumn configuration (A, C, D) and a winter configuration (B, B1). Observations also confirm differences in the amplitude of seasonal variation of the thickness of the upper layer over and outside the LV presented in MIT GCM. Specifically, the observed summer to winter mean variation of the mixed layer depth in the Lofoten Basin is from 50 to 200-400 m (Nilsen and Falck, 2006, Rossby et al., 2009), while over the LV itself is reaches 500-600 m (Alekseev, 1991; Nilsen and Falck, 2006). The difference is also indirectly confirmed by an observed two-fold amplitude difference of seasonal variation of the depth of the upper ocean isopycnals: in the center of the Lofoten Basin (where the LV is situated) as compared to that along the basin boundaries (Rossby et al., 2009).

Observations and MIT GCM data suggest moderate variations of dynamic characteristics of the LV, episodically re-generated during merger or winter convection events. A gradual decrease of the LV dynamic parameters by about 3% per month in-between the regeneration events, detected in MIT GCM results, suggests a decay time of order of 2-3 years. Calculations presented by Søiland and Rossby (2013) indicate that small-scale turbulent diffusion gives characteristic decay times of dozens of years. In this paper we investigated the alternative mechanism of vortex dynamic instability, often considered to be one of the principal mechanisms for decay of mesoscale eddies (Carton, 2001; Cushman-Roisin and Beckers, 2011). In Section 3.4 it was noted that the LV vertical and horizontal structure satisfies the necessary condition for vortex dynamic instability (Sokolovskiy, 1997b; Cushman-Roisin and Beckers, 2011), and the observed range of Ro (0.03-0.15) and Bu (0.05-0.1) numbers suggest that baroclinic or mixed instability can efficiently develop (Ripa, 1992, Carton et al., 2014; Cohen et al., 2015).

An example of development and propagation of the LV perturbations of the 2nd azimuthal mode, observed in the MIT GCM is presented in Fig. 23. The period of rotation of the perturbation is around 20 days and the phase speed of the perturbation is around 12 cm s^{-1}. This is about 3 times less than the maximum azimuthal velocity (40 cm s^{-1}) of the vortex. This ratio corresponds well to that of a baroclinically-unstable azimuthal mode-2 propagating around an anticyclonic eddy (Paldor, 1999).

In the realistic MIT GCM model the LV, most of the time, keeps away from the steep basin boundaries, which may deform and force stripping of the vortex. The LV, though, often interacts with other finite-amplitude eddies, both cyclones and anticyclones. However, the direct effect of stripping of a part of the LV skirt by the current shear due to presence of other eddies is not observed during such interactions. Following model results (for example, Ciani et al., 2016), we consider the LV to be affected by another eddy after the distance between their centers becomes less than 3 LV radii. Then, the typical time of contact of the LV with other eddies is of order of 2-4 weeks, while the instability develops over 5-8 months, a much longer time scale. The perturbations at the LV boundary continue developing even when there is no direct contact with other eddies. For example, in Fig. 23, rotation of perturbations around the LV occur while eddies around keep relatively stationary positions or move away from the LV. Therefore, we assume that relatively slowly developing dynamic instability to be the main reason for gradual decay of the LV in-between the re-generation events. Contact with other eddies may trigger instability of the LV which then develops further, fed by the LV energy.

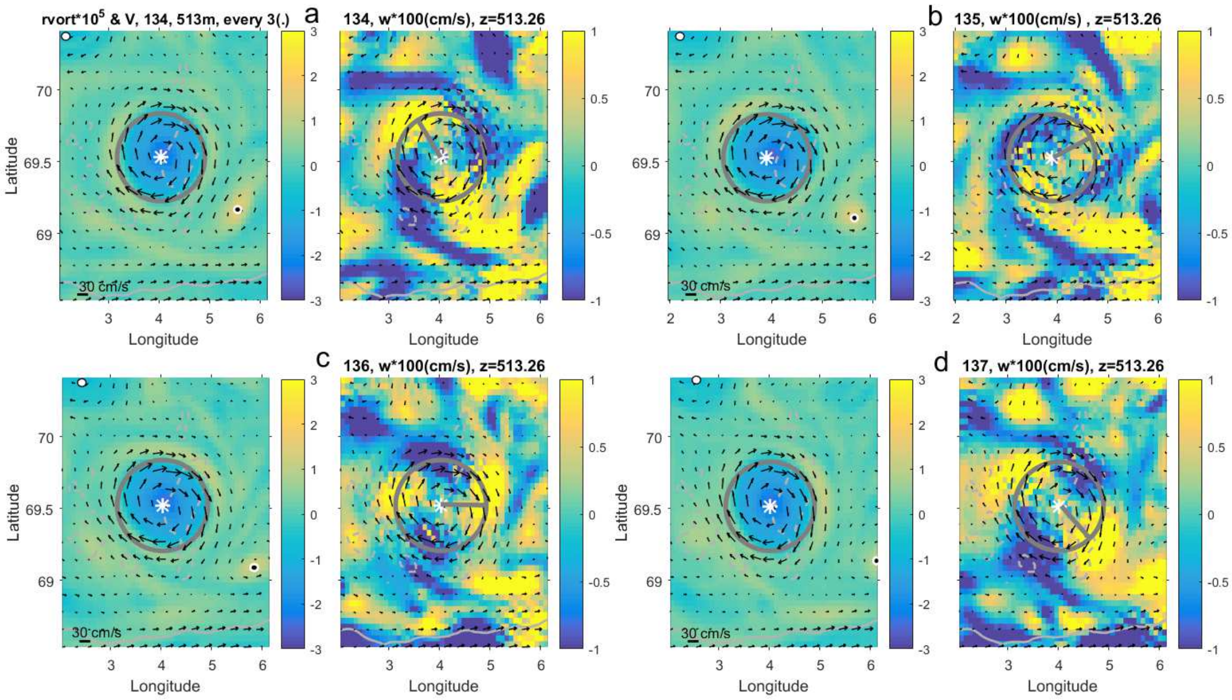

Fig. 23. Relative vorticity (x10^{-5} s^{-1}, left panels) and vertical velocity (x10^{-2} cm s^{-1}, right panels) at 513 m depth for four consecutive moments of time (a, b, c, d) with the time interval between panel sets of 3 days. White star marks the LV center, grey circle marks the LV dynamic radius, and grey segment starting at the LV center – the position of maximum of vertical velocity of perturbations of the second azimuthal mode. Black point with white circle and white point with black circle mark a cyclone and an anticyclone in the vicinity of the LV.

To observe how the dynamic instability develops in the LV, a detailed analysis of the LV stability properties has been done with linear and non-linear QG models. In these models we used a simplified LV structure, based on the analysis of MIT GCM results in Sections 3.1-3.2: the 3-layer ocean, where the LV is approximated by patches of constant PV. Series of experiments with an artificially perturbed vortex with the predefined perturbations intensity and the motionless flat-bottom ocean (Section 3.4), and with an initially unperturbed vortex and the realistic mean flow and varying bottom topography (Section 3.5) are conducted. The first series of experiments show that the LV is baroclinically unstable, and that baroclinic instability can split the original vortex into parts within 4-8 months (Section 3.4). Even in relative simplicity of the QG model, the development of perturbations in the LV fairly well agrees with the MIT GCM realistic simulations on several key features. As in the primitive equation model, the QG models (Section 3.4) predict relatively slow development of the instability in the LV - of order of several months. The slightly higher rates of LV decay are observed in the upper and the lower layers, compared to the middle (core) layer. This can be explained by a much stronger radial PV gradient at the core levels, which forms a barrier for the particle exchange between the LV core and the surrounding fluid. Also, similar to the primitive equations model, the QG models suggest a dominance of the azimuthal modes $m = 2$, 3, 4 for the most typical configurations of the vertical PV structure in the LV.

However, important differences are also observed. A notable discrepancy between the QG models over a flat bottom and the primitive equation model is a difference in the LV volume loss as a result of the development of perturbations. In the small-amplitude linear and the finite-amplitude non-linear flat-bottom QG simulations, over half of the initial LV volume is expected to be dispersed by the instabilities within 4-8 months (Section 3.4). For large-amplitude mode-3 initial perturbations, the LV in the upper layer breaks up into 4 eddies (including the remains of the LV core) of nearly equal size already within about 3 months, and the vortex completely disintegrates within 5 months. The overall rate of the core decay is thus 20-30% per month. The MIT GCM simulations, only the strongest instability events lead to a notable volume loss from the LV core, and this loss does not exceed 10-20% of its initial volume (Fig. 22).

Differences in development of instability between the full-complexity primitive equation model and the linear QG model are not surprising since perturbations experienced by the LV cannot be considered small-amplitude. But the differences between the primitive equation model and the non-linear QG model are less obvious and demand more investigation. As mentioned in the introduction, at low Rossby numbers (0.1 in the LV) and low vortex-core thickness ratio to water depth ($\nu = h_{2,LV} / H$ =0.20-0.25 in the LV) the hybrid (Rossby-Kelvin wave) and the baroclinic (Rossby wave) instabilities may arise (Ripa, 1992), as well as the barotropic instability. The first type can exist in the primitive equation model, but not in the QG model, while the second and the third types may be generated in both models. And yet, instability in the primitive equation model appears to develop much slower and never results in a significant decrease of the vortex core volume.

There may be several reasons for this. An obvious one is the difference in the vertical PV structure in and around the vortex in the 3-layer QG model and in the 50-layer MIT-GCM. In particular, when the PV gradient is zero in a layer, this layer does not support development of Rossby waves. Therefore baroclinic, hybrid and Sakai instabilities cannot develop intensive perturbations in this layer. In the limiting case of the 2-layer QG model, the vortex then becomes stable to any external perturbations, independent of weather it is a sea-surface or a mid-depth intensified vortex (Dewar and Killworth, 1995; Benilov, 2004; Cohen et al., 2015a;

Sutyrin, 2015; Cohen et al., 2016). In the 3-layer QG model used in Section 3, a small radial PV gradient in the lower layer (on average only 5% of that at the level of the LV core) is still sufficient for supporting Rossby wave instabilities, as it is shown by the numerical experiments. In a realistic vortex, such a ‘compensation’ layer can be formed below or above the vortex core, where the anticyclonic rotation is balanced by compression of isopycnals. In the 50-layer MIT GCM the radial PV gradient changes sign above and below the LV, and isopycnic layers with a very weak or zero PV gradients do exist. Inside these comparatively thin layers the amplitudes of Rossby waves decrease exponentially from the layer boundaries, reducing coupling between the layers (Sutyrin, 2015). Therefore, one could argue, the simplified 3-layer PV structure in the QG model is able to support overall higher rates of development of baroclinic instability, as compared to MIT GCM.

Furthermore, it has been numerically observed that, under certain conditions, non-linear effects may stabilize linearly-growing perturbations even though sufficient instability conditions are met (Sutyrin, 2015). Thus, for vortex instability in a QG model, a non-linear saturation of growing finite-amplitude perturbations on elliptical vortices have been observe (Flierl, 1988; Ripa, 1992). Even being present in the non-linear QG and in the primitive equation models, details of the non-linear evolution may differ between both models (Boss et al., 1996). For example, it is expected that frictional effects and the turbulent environment result in a faster damping of perturbations in the primitive equation model, as compared with the QG model.

A QG experiment with more realistic background conditions (Section 3.5) showed, that adding the large-scale gently sloping topography (around 1 m km^{-1}) and the barotropic mean flow (of 10 cm s^{-1}), as observed in the Lofoten Basin, reduce the LV decay rate, brining it closer to that in the MIT GCM. The time for instability to penetrate into the vortex core and to break it into separate vorticity patches in the QG model now increases to 1 year (Fig. 20). Sloping topography is particularly important, as an experiment with the mean flow and a localized topographic depression (Appendix B) rather show a decrease in the LV decay time (2-5 months, Fig. B1), as compared to the motionless flat-bottom background case. Overall, steep topographic features are known to trigger instability in oceanic vortices, and even their breakdown (Thierry and Morel, 1999; Van Geffen and Davies, 2000; Richardson et al., 2000; Bashmachnikov et al., 2009), and the increase in the time of the eddy decay over a sloping bottom has not been expected. A possible reason is that the PV variations due to topography forces mode 1 in the vortex perturbation (Fig. 20), which decays at a lower rate extracting energy from the faster decaying modes 2-4. Further experiments are required to study this phenomenon.

A difference in the area of concentration of the perturbation energy is also noted. In contrast to the nonlinear QG model (Section 3.4), where instability penetrates deep into the LV core and splits up the vortex of nearly equal size within a few months, instability in MIT GCM typically develops only within the skirt of the vortex. It results in separation of elongated filaments and small (submsoscale) relative vorticity patches (Section 3.6). The latter is consistent with the development of baroclinic instability observed in a primitive equation model of eddies with low Burger numbers (Mahdinia, et al., 2016). Stripping of the skirt of an oceanic mesoscale vortex, as a result of baroclinic instability, has also been observed in the ocean and supported by numerical model studies (Ménesguen et al., 2012). The general effect of stripping of an eddy skirt in an external strain field has also been observed in some model studies (Maximenko and Orlov, 1991; Mariotti et al., 1994).

In the MIT GCM weak background current and other eddies yield the main source of strong localized velocity shear around the LV. Such interactions can suppress development of instabilities in the vortex core (Dewar and Killworth, 1995). In fact, in Section 3.6 we noted that the intensity of the external strain (strongly intensified as the LV interacts with other eddies) is negatively correlated with the intensity of the perturbations at the LV boundary. It can be speculated that external strain formed at the vortex boundary is responsible for concentration of energy of the developing instabilities at the outer part of the vortex patches, and remove the energy of growing perturbations before they penetrate deep into the core. Further wrapping of these filaments around the vortex may prevent the core from breaking into larger fragments.

In our MIT GCM simulations, during the in most of the events of filamentation, the volume of the LV core does not vary as a result of development of instability. This is not the case for the kinetic energy and angular momentum of the LV core, clearly affected by the development of the perturbations in this model. Thus, in the present study, a significant negative correlation (-0.7 to -0.8) between the intensity of the azimuthal disturbances and the mean relative vorticity of the core is detected (for annual sliding means). Therefore, after the filaments separate from the skirt, removing angular momentum, the original radial momentum distribution is restored via translation of the angular momentum outwards from the core. These variations in redistribution of dynamic properties within the LV core are not reproduced in the QG models, considering dynamics of patches of homogenous PV.

Another discrepancy between the QG models (section 3.4) and the primitive equation model (Section 3.6) is the structure of the perturbation of the LV. In the QG models the rate of development of the first four azimuthal perturbation modes are rather close, but the 3rd mode is predicted to be the most unstable (Table 3). In contrast, the 2nd azimuthal mode is dominating the LV perturbations in the MIT GCM, although the 3rd and the 4th modes are also pronounced. This development of the perturbations in the LV in MIT GCM ends in ejection of mostly two instability filaments, while three instability filaments are ejected during only a few events. For a vortex structure similar to that of the LV, the dominance of the 2nd azimuthal mode, during development of the baroclinic and the mixed instabilities in a primitive equation model, was also obtained in Mahdinia, et al. (2016).

A possible reason may be the single-mode predictions of the QG model experiments, which do not capture possible non-linear energy exchange between a set of different equally strong modes during the initial stages of their development. With the observed close rate of development of the first four azimuthal modes in MIT GCM, interactions between different modes may lead to a faster growth of one mode at the expense of others. The difference between the models may also result from the simplification of the LV vertical structure in the QG models. Thus, in a study of mid-depth anticyclonic eddies with a 5-layer linear QG model, Carton et al. (2014) showed that for large eddies (R on order of 2-5 R_d , as in the case of the LV) the 3rd azimuthal mode is the most unstable one. However, experiments with a continuously stratified QG model (Nguyen et al., 2012) have also shown that the 3rd or the 4th azimuthal modes start dominating over the 2nd mode only as the eddy Burger number falls below 0.07-0.08. As the LV Bu ~0.05-0.10, in the more realistic continuous-stratification conditions, either the 2nd or the 3rd azimuthal modes are expected to dominate (see also Baey and Carton, 2002).

Finally, in the full-complexity of MIT GCM model, interactions with other eddies are observed to primarily force elliptic deformations (the 2nd azimuthal mode) in the LV. The interaction with cyclones can also force perturbation of the 1st azimuthal mode (Carton et al., 2014). Although the latter is not observed to develop to large amplitudes in the LV, it can have indirect effects on the neighboring modes in the MIT GCM: (a) the forced mode can alter the radial distribution of intensity of the LV perturbations, driving them away from the most unstable normal mode and slowing down their growth; (b) the nonlinear wave-wave interactions of mode 1 with mode 3 may force Additionally, Volkov et al. (2013) identified dipole and quadrupole wave patterns in the Lofoten Basin as 1st and 2nd modes of topographic Rossby waves in a bottom depression. Interaction of the LV with the instantaneous circulation structures, formed by the Rossby waves, can trigger the development of the corresponding azimuthal modes in the LV.

We have noted a range of differences between the LV decay in QG and primitive equation calculations. A common and key finding is that that perturbations at the LV boundary do not develop to penetrate deep into the LV core to cause the vortex breakdown, contrary to what was observed in QG simulations with the motionless flat-bottom background. Adding a realistic background current and single a step-like bottom depression show a similar or even faster decay rate. Adding a realistic background current and a gently sloping bottom topography decrease the LV decay rate, bringing the QG simulations closer to those of MIT GCM. However, either the development of the baroclinic instability in Section 3.4 or a mixed baroclinic-barotropic instability in Section 3.5 result in a relatively long decay time of the LV, over 5-12 months, for external forcing, notably eddy mergers or deep convection in the core region, to interrupt the development of the instability and re-build the LV. Further experiments will be conducted to deeper investigate the mechanisms governing the LV decay.

Volkov et al. (2015) analyzed components of the relative vorticity balance for the same MIT GCM model fields. The authors found that time variations of the relative vorticity of the LV core are principally correlated with the intensity of eddy fluxes of relative vorticity through the LV boundaries, and suggested that winter convection should be of minor importance in restoring the LV. In this study it is demonstrated that the LV barotropic and the baroclinic potential energy anomalies clearly intensify, both during mergers and winter convection events, while the LV integral kinetic energy is not always affected. We also observe that the LV relative vorticity does not always increase after a merger (the LV-integrated angular momentum typically does). Meanwhile, it was demonstrated that, on the annual time scale, the LV relative vorticity and its volume strongly correlate with the intensity of the detected wave-like perturbations, rather than with the number merges per year. It is also noted that the LV volume/intensity are restored a few months after the minimum relative vorticity of the core is reached, even when no merger or deep winter-spring convection are detected. The detailed mechanisms governing the LV re-generation thus remain to be further investigated.

Appendix A

Under the QG approximation without external forcing, the conservation of PV (Π) hold true within each layer (Pedlosky 1987).

$$d_j \Pi_j / dt = 0,$$

where $d_j / dt = \partial / \partial t + u_j \partial / \partial x + v_j \partial / \partial y$.

The three-dimensional potential vortex $\vec{\Pi}$ is related to the hydrodynamic pressure perturbation relative to the hydrostatic-equilibrium pressure ($\vec{p}$) by the linear differential operator:

$$\vec{\Pi} = \nabla^2 \vec{p} + T\vec{p}, \qquad \text{(A.1)}$$

$$\vec{\Pi} = \begin{pmatrix} \Pi_1 \\ \Pi_2 \\ \Pi_3 \end{pmatrix}, \qquad \vec{p} = \begin{pmatrix} p_1 \\ p_2 \\ p_3 \end{pmatrix}, \qquad T = \begin{pmatrix} -\dfrac{F_1}{h_1} & \dfrac{F_1}{h_1} & 0 \\ \dfrac{F_1}{h_2} & -\dfrac{F_1+F_2}{h_2} & \dfrac{F_2}{h_2} \\ 0 & \dfrac{F_2}{h_3} & -\dfrac{F_2}{h_3} \end{pmatrix},$$

where $\nabla^2 = \partial^2 / \partial x^2 + \partial^2 / \partial y^2$, $F_1 = (fL)^2 / g_1^{'} H$ and $F_2 = (fL)^2 / g_2^{'} H$ are Froude numbers, $g_1^{'} = g(\rho_2 - \rho_1) / \rho_0$, $g_2^{'} = g(\rho_3 - \rho_2) / \rho_0$); f is the constant Coriolis parameter, g is the acceleration due to gravity, ρ_0 is the mean density value, L is the horizontal scale and H is the vertical scale, such that the depth of ocean equals to $H(h_1 + h_2 + h_3)$, where h_1, h_2, h_3 are the non-dimensional depths of the upper, the middle end the lower layers, respectively ($h_1 + h_2 + h_3 = 1$).

A diagonalization method, described in detail in (Kamenkovich et al., 1982), transforms Eq. (A.1) to:

$$\vec{W} = \nabla^2 \vec{w} + U\vec{w}, \qquad \text{(A.2)}$$

where $\vec{W} = S\vec{\Pi}$, $\vec{p} = Q\vec{w}$, $U = \lambda E$,

$$Q = \left(\vec{q}^{\,(1)}, \vec{q}^{\,(2)}, \vec{q}^{\,(3)}\right) = \\ = \begin{pmatrix} 1 & \dfrac{h_3 \lambda_3}{\lambda_3 - \lambda_2} & -\dfrac{F_1}{h_1 \lambda_3} \\ 1 & \dfrac{1}{\lambda_3 - \lambda_2}\left(h_2 \lambda_3 + \dfrac{F_2}{h_2}\right) & -\left(\dfrac{F_1}{h_1 \lambda_3} + 1\right) \\ 1 & \dfrac{1}{\lambda_3 - \lambda_2}\left[h_2 \lambda_3 + \dfrac{F_2}{h_2} + \lambda_2 + \dfrac{F_1 (h_1 + h_2)}{h_1 \lambda_2}\right] & -\left[\dfrac{F_1}{h_1 \lambda_3} + 1 + \dfrac{h_2}{F_2}\left(\lambda_3 + \dfrac{F_1 (h_1 + h_2)}{h_1 \lambda_2}\right)\right] \end{pmatrix}, \qquad \text{(A.3)}$$

$$S = Q^{-1} =$$

$$= \begin{pmatrix} h_1 & h_2 & h_3 \\ -\frac{h_2}{F_2}\left[\lambda_3 + \frac{F_1(h_1+h_2)}{h_1 h_2}\right] & \frac{h_2}{F_2}\left[\lambda_3 + \frac{F_1(h_1+h_2)+F_2 h_1}{h_1 h_2}\right] & -1 \\ -\frac{1}{\lambda_3-\lambda_2}\left[\lambda_2 + \frac{F_1(h_1+h_2)}{h_1 h_2}\right] & \frac{1}{\lambda_3-\lambda_2}\left[\lambda_2 + \frac{F_1(h_1+h_2)+F_2 h_1}{h_1 \lambda_2}\right] & -\frac{1}{\lambda_3-\lambda_2}\frac{F_2}{h_2} \end{pmatrix}, \tag{A.4}$$

$$\lambda_1 = 0; \quad \lambda_{2,3} = -\frac{1}{2}\left[\frac{F_1}{h_1} + \frac{F_1+F_2}{h_2} + \frac{F_2}{h_3} \mp \sqrt{\left(\frac{F_1}{h_1} + \frac{F_1+F_2}{h_2} + \frac{F_2}{h_3}\right)^2 - 4\frac{F_1 F_2}{h_1 h_2 h_3}}\right].$$

Here λ_j are the eigenvalues of the spectral equation $T\vec{q} + \lambda\vec{q} = 0$ and $\vec{q}^{(j)}$ $(j = 1,2,3)$ are its eigenvectors, E is an identity matrix. The model is solved under the rigid-lid condition. Therefore, the eigenvalue of the barotropic mode ($j = 1$) is zero. In any point (x, y) the components w_j of the auxiliary vector $\vec{w}$ from the right-hand part of equation (A.1) can be determined with the use of Green function G_j :

$$w_j(x,y) = \int\limits_{-\infty}^{+\infty}\int W_j G_j(r)\,dx'dy', \quad G_j = \frac{1}{2\pi}\begin{cases} \ln\gamma^* r, & j = 1, \\ -K_0(\gamma_1 r), & j = 2, \\ -K_0(\gamma_2 r), & j = 3, \end{cases} \tag{A.5}$$

where $r = \sqrt{(x-x')^2 + (y-y')^2}$, $\gamma_{1,2} = \sqrt{-\lambda_{2,3}}$ and $K_0(z)$ is the modified Bessel function of order 0 (hereinafter, without a special mention, we shall also use the modified Bessel functions of order n $K_n(z)$ and $I_n(z)$).

Let us suppose, that the potential vorticities W_j are piecewise-constant functions of the type

$$W_j = \Pi_j\,\chi(\sigma_j), \quad \chi_j = \begin{cases} 1 & inside\ \sigma_j \\ 0 & outside\ \sigma_j \end{cases}, \qquad j = 1,2,3, \tag{A.6}$$

where $\overline{\Pi}_j$ are constant and areas σ_j initially represent the circles with the radii R_j . Following Sokolovskiy (1991), we can then write the expressions for the pressure in the layers:

$$p_j(x,y,t) = \Pi_j \oint\limits_{C_j(t)} M(r)\,N\,d\nu_j + \sum_{k=2}^{3} q_{jk} \sum_{m=1}^{3} \Pi_m s_{km} \oint\limits_{C_m(t)} M_{k-1}(r)\,N\,d\nu_m, \quad j = 1,2,3. \qquad \text{(A.7)}$$

Here, as before, $r = \sqrt{(x-x')^2 + (y-y')^2}$, but now x' and y' are the coordinates of the points of integration located on the contours C_j of initially circular vortex patches σ_j; $\nu_j(x',y')$ is a parameter continuously varying counterclockwise along the contour C_j ; $M(r) = r^2(\ln r - 1/2)/4\pi$, $M_n(r) = (\gamma_n\, r\, K_1(\gamma_n\, r) - 1)/2\gamma_n, (n = 1,2)$, $N = [(x'-x)(\partial y'/\partial \nu_j) - (y'-y)(\partial x'/\partial \nu_j)]/r^2$ and q_{jk}, s_{jk} are the elements of matrices Q, S from (A.3) and (A.4).

The equations (Eq. A.7) form a theoretical basis for the so-called Contour Dynamic Method (Zabusky et al, 1979) and demonstrate that, for the assumptions made, perturbations of pressure (streamfunction) in each of the fluid layer j are fully determined by an evolving configuration of the boundaries of the vortex patch C_j. This equation set can be solved numerically with a three-layer version of the Contour Dynamics Method (Sokolovskiy 1991, Sokolovskiy and Verron, 2014).

It is easy to obtain from (Eq. A.7) that the appropriate distributions of azimuth velocities have the form:

$$V_j(r) = \sum_{k=1}^{3} q_{jk} \sum_{l=1}^{3} \Pi_l s_{kl} H_{k-1}^{(l)}(r), \quad j = 1,2,3,$$

where

$$H_0^l(r) = \frac{1}{2}\begin{cases} r/R_l, & r \le R_l \\ R_l/r, & r > R_l \end{cases} \quad l = 1,2,3,$$

$$H_n^l(r) = \frac{1}{2}\begin{cases} K_1(\gamma_n R_l) I_1(\gamma_n r), & r \le R_l \\ K_1(\gamma_n r) I_1(\gamma_n R_l), & r > R_l \end{cases}, \quad n = 1,2; \quad l = 1,2,3.$$

The general scheme of stability analysis for an axisymmetric three-layer vortex with relatively small azimuthal perturbations in the shape of the vortex patches forming the vortex is presented below. Following (Sokolovskiy 1997a, 1997b) let us represent the contours C_j, which are the lines of constant potential vorticities in polar coordinates (r,θ), in the parametric form:

$$f_j(\theta,t;R_j)=R_j\left[1+\varepsilon_j\exp[im(\theta-\delta t)]\right],\quad \varepsilon_j<<1,\quad j=1,2,3. \qquad \text{(A.8)}$$

Here, PV perturbations of amplitude $\overline{\Pi}_j$ (see Eq. A.6) of an azimuthal mode number $m\geq 1$ are superimposed on the unperturbed state in the area $R_j\pm\varepsilon_j$. The imaginary part of the complex number δ defines time evolution of the amplitude of the azimuthal mode m. The total differentiation of (Eq. A.8) with the respect to time gives us the set of equations:

$$f_j f_{jt}+V_j^{(\theta)}f_{j\theta}-V_j^{(r)}f_j=0,\quad j=1,2,3, \qquad \text{(A.9)}$$

where $V_j^{(\theta)}$ and $V_j^{(r)}$ are the azimuthal and the radial components of velocities in the j th layer, and the subscripts t and θ denote partial differentiation with the respect to the appropriate variables.

Taking into account Eq. (A.8), we perform a linearization of Eq. (A.9) and obtain a system of linear algebraic equations for the small amplitude perturbations (see details in Sokolovskiy, 1997a, 1997b). The system reduces to the set of characteristic equations:

$$\left|B-\delta E\right|=0 \qquad \text{(A.10)}$$

Here matrix B contains terms:

$$b_{nj}=\sum_{k=1}^{3}s_{kn}\left[q_{nk}T_{nk}^{(k-1)}-\Delta_{nj}\frac{m}{R_j}U_{k-1}(R_j)\right],\quad n,j=1,2,3.$$

Here Δ_{nj} is Kronecker delta-symbol; $T_{nn}^{(0)}=1/2$, $T_{nn}^{(1,2)}=mI_n(\gamma_{1,2}R_j)K_n(\gamma_{1,2}R_j)$, $(n=1,2,3)$. Note that coefficients of the system of equations (Eq. A.10) depend on all external parameters, as they contain the terms from matrices (Eq. A.3) and (Eq. A.4). Expressions for the variables U_j and $T_{nk}^{(j)}$ at $n\neq k$ depend on the shape of the vortex under study and have a lengthy form. For the case $R_1\geq R_2\geq R_3$, these expressions are presented in (Sokolovskiy 1997a, 1997b). From (A.8) it follows that the instability condition for a mode number m is determined by the inequality $\operatorname{Im}\delta>0$, which occurs only if exists a single real root of the cubic equation for δ in Eq. (A.9).

Appendix B

In section 3.4 the LV was simulated as an idealized vortex over flat topography and with zero background flow. Here we will study the vortex in more realistic conditions.

The general shape of the bottom of Lofoten Basin, deepening to southwest, is simulated with 2 not-concentered circular bottom depressions of 3040 m (yellow filled circle in Fig. B1) and 3080 m (green filled circle in Fig. B1) depths with the diameters of 200 and 90 km, respectively. A northeasterly barotropic mean flow with the initial velocity of 52 cm s^{-1} is imposed to simulate the western and eastern branches of the NwAC (Fig. 1). Observations (Skagseth et al. 2008) and the MIT GCM model results (not shown) suggest that the NwAC reaches ocean bottom, having a pronounced barotropic component.

A barotropic north-easterly mean flow (taken $U_0 = V_0 = 52$ cm s^{-1} at infinity) and normalized bottom elevations over 3000 m, negative for a depression (σ_i, $i = 1, 2$) added, new terms appear on the right-hand side of (A.7), described by equation (5). As in Appendix A, evolution of the contours, limiting the areas of constant PV in each of the layers (Π_j), is estimated by numerical evaluation of displacements of its nodes for the total pressure field, defined above.

The upper left panel in Figure B1 shows the background and initial conditions. Specifically, the mean flow forms closed isolines of cyclonic circulations (inside the thick black drop-like structure), roughly reminding what is observed in the Lofoten Basin (Fig. 1). The LV is immersed in the flow inside the green contour (Fig. B1, upper left panel). In this case, contrary to Appendix 1, the instability of the LV is not imposed, but is generated by the external combination of the topographic and the mean-flow.

The remaining panels show the evolution of instability. There is clear sign of topographic trapping of both the vortex and the filaments emerging from instability. A significant distortion of the main core with a further loss of the LV to eddies and filaments occur after model time 5-8, e.g. 2-3 months after the beginning of the simulations. By the fifth month of the simulations (t=12.5), the LV core nearly totally destroyed, except for the middle layer, where it is spilt in several smaller structures. This study, even if simplified, demonstrates that the even if LV is over one of topographic depressions of the central part of the Lofoten Basin, it cannot stabilize the LV.

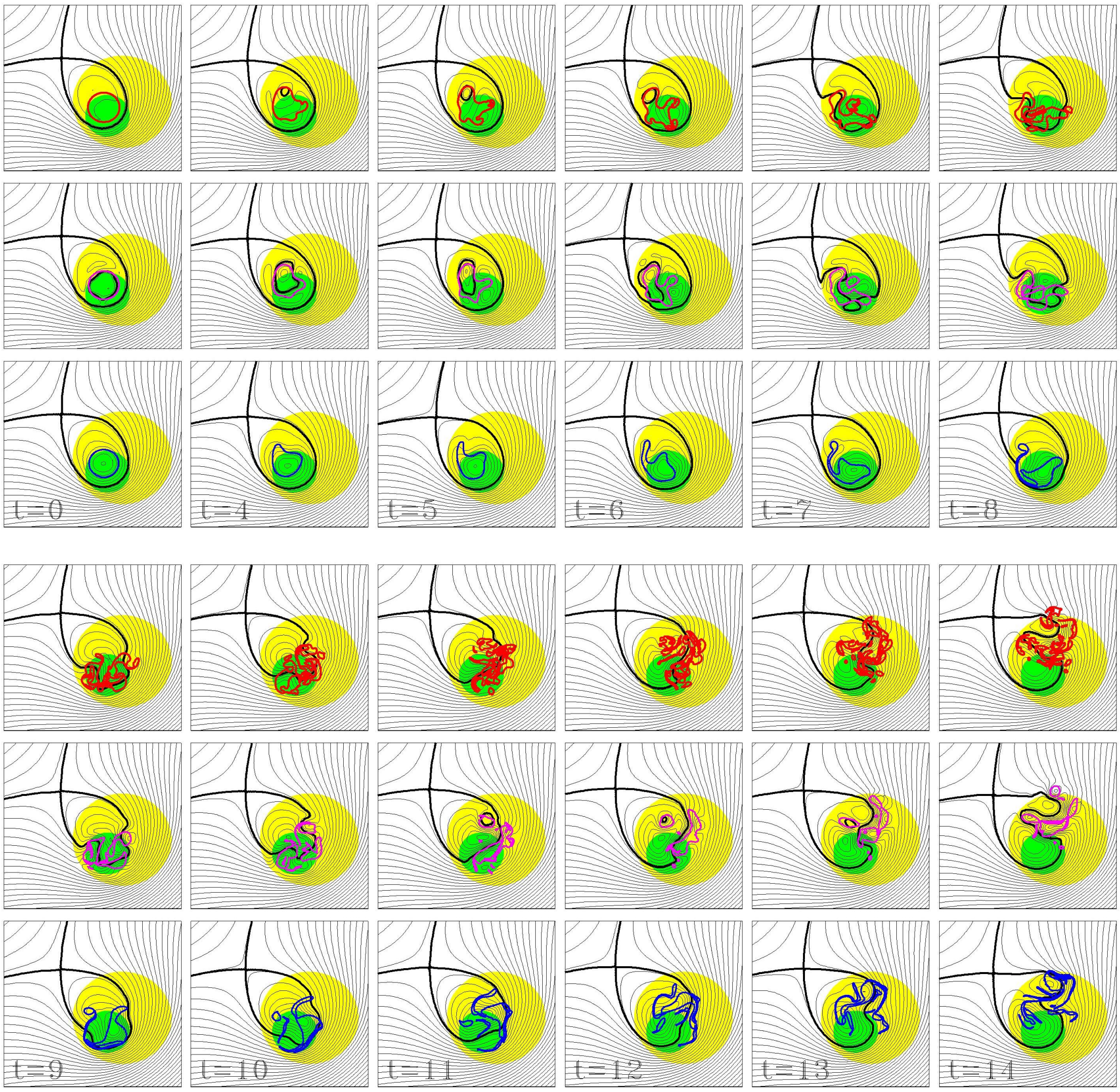

Fig. B1. Simulations of the LV evolution in a QG model, when a barotropic background flow and varying bottom topography are included. Water depth in the white area is 3000 m, yellow area – 3040 m (the diameter of the circle area is 200 km) and green area – 3080 m (the diameter of the circle area is 90 km). Gray contours are the streamlines of the zonal and the meridional components of current velocity. Black line marks the separatrix at each time step. This limits the area, where particles are not advected out of the simulation region. The LV is initially centered in the elliptic point of the mean flow configuration. The dimensionless time unit in each of the 3-panel column corresponds to 12 days. Each frame shows vortex patches in the upper (red upper contour plots in a plate), middle (magenta middle contour plots in a plate) and lower (blue lower contour plots in a plate) layers as function of non-dimensional time.

Acknowledgements

The authors acknowledge the Saint Petersburg State University (Russia) for the research grants IAC N 18.38.142.2014 (MIT simulations), I.B. also acknowledges support of the Université de Bretagne Occidentale and LabexMER project and the MARE - Marine and Environmental Sciences Centre of the University of Lisbon (CO-Pest-OE/MAR/UI0199/2011) (analysis of LV vertical structure in MIT simulation results). Computational resources and support from the NASA Advanced Supercomputing (NAS) Division are gratefully acknowledged. For several experiments computer resources were provided by Resource Center "Computer Center of SPbU" (http://cc.spbu.ru). I.B. was supported by RFBR project 16-05-00452 (analysis of the LV dynamics in MIT simulation results). M.A.S. was supported by Russian Science Foundation (grant N 14-50-00095, application to ocean) and Ministry of Education and Science of the RF (grant N 14.W.03.31.0006, numerical simulation). The work of M.A.S. and X.C. was also performed in the frame of Russian-French project PRS from RFBR/CNRS (grant N 16-55-15001/1069, applications to ocean with sloping topography). D.L.V was supported by the NASA Physical Oceanography program (Grant NNX11AE27G) and by the base funds of NOAA Atlantic Oceanographic and Meteorological Laboratory. P.E.I. was supported by the Norwegian Research Council projects NorSEE (221780) and ProVoLo (250784). Wavelet software was provided by C. Torrence and G. Compo and is available at URL: http://paos.colorado.edu/research/wavelets/.

References

Adcroft, A., Hill, C., Marshall, J., 1997. The representation of topography by shaved cells in a height coordinate model. Mon. Weather Rev. 125, 2293–2315.

Alekseev, G.V., M.V. Bagryantsev, P.V. Bogorodskiy, V V. Vasin, and P. E. Shirokov, 1991. Structure and circulation of water in the area of anticyclonic eddy in the northeastern Norwegian Sea [in Russian], Probl. Arctic Antarct. 65. 14–23.

Antonov, J.I., Seidov, D., Boyer, T.P., Locarnini, R.A., Mishonov, A.V., Garcia, H.E., Baranova, O.K., Zweng, M.M., .Johnson, D.R., 2010. World Ocean Atlas 2009, Vol. 2: Salinity. S. Levitus, Ed. NOAA Atlas NESDIS69, U.S. Government Printing Office, Washington,D.C., 184 pp.

Baey, J.-M., Carton, X., 2002. Vortex multipoles in two-layer rotating shallow-water flow. J. Fluid Mech., v. 460, pp. 151-175.

Bashmachnikov, I., C. Mohn, J. L. Pelegrí, A. Martins, F. Machín, F. Jose, and M. White, 2009. Interaction of Mediterranean water eddies with Sedlo and Seine seamounts, Subtropical Northeast Atlantic. Deep-Sea Research II, 56, 2593–2605.

Bashmachnikov, I., Neves, F., Calheiros, T., Carton, X., 2015. Properties and pathways of Mediterranean water eddies in the Atlantic. Progress in Oceanography, 137, 149-172.

Benilov, E.S., Broutman, D., Kuznetsova, E.P., 1998. On the stability of large-amplitude vortices in a continuously stratifed fuid on the f-plane. J. Fluid Mech. v. 355, pp. 139-162.

Benilov, E.S., 2000. The dynamics of a near-surface vortex in a two-layer ocean on the beta-plane. J. Fluid Mech. 420, 277-299.

Benilov, E.S., 2001. Baroclinic instability of two-layer flows over one-dimensional bottom topography. J. Phys. Oceanogr. 31, 2019-2025.

Benilov, E.S., 2003. Instability of quasi-geostrophic vortices in a two-layer ocean with a thin upper layer. J. Fluid Mech. 475, 303-331.

Benilov, E.S., 2004. Stability of vortices in a two-layer ocean with uniform potential vorticity in the lower layer. J. Fluid Mech. 502, 207-232.

Benilov, E.S., 2005a. Stability of a two-layer quasigeostrophic vortex over axisymmetric localized topography. J. Phys. Oceanogr. 35, 2019-2025.

Benilov, E.S., 2005b. On the stability of oceanic vortices: A solution to the problem? Dyn. Atmos. Oceans. 40, 133-149.

Björk, G., Gustafsson, B.G., Stigebrandt, A., 2001. Upper layer circulation of the Nordic seas as inferred from the spatial distribution of heat and fresh water content. PolarRes. 20, 161–168.

Blindheim, J, Rey, F., 2004. Water-mass formation and distribution in the Nordic Seas during the 1990s. ICES Journal of Marine Science. 61 (5). P. 846–863, doi: 10.1016/j.icesjms. 2004.05.003.

Boss, E., Paldor, N., Thompson, L., 1996. Stability of a potential vorticity front: from quasi-geostrophy to shallow water. J. Fluid Mech., 315, 65-84.

Boyer, T. P., Levitus, S., Antonov, J.I., Locamini, R.A., and Garcia, H.E., 2005. Linear trends in salinity for the World Ocean, 1955–1998. Geophys. Res. Letters, 32(1), L01604.

Carton, X. J., 1992. On the merger of shielded vortices. EPL (Europhysics Letters), 18(8), 697.

Carton, X.J., McWilliams, J.C., 1989. Barotropic and baroclinic instabilities of axisymmetric vortices in a QG model. In: Nihoul, J.C.J., Jamart, B.M. (eds.) Mesoscale/Synoptic Coherent Structures in Geophysical Turbulence, Liège 1988 International Colloquium on Ocean Hydrodynamics, vol. 50, pp. 225–244. Elsevier Oceanographic Series, Amsterdam.

Carton, X.J., Corréard, S.M., 1999. Baroclinic tripolar vortices: formation and subsequent evolution. In: Sorensen, J.N., Hopfinger, E.J., Aubry, N. (eds.) Simulation and Identification of Organized Structures in Flows, IUTAM/SIMFLOW1997 Symposium in Lyngby, pp. 181–190. Kluwer, Dordrecht.

Carton, X., Flierl, G.R., Perrot, X., Meunier, T., Sokolovsiy, M.A., 2010a: Explosive instability of geostrophic vortices. Part 1. Baroclinic instability. Theor. Comp. Fluid Dyn., 24, 125-130.

Carton, X., Maze, G., Legras, B., 2002. A two-dimensional vortex merger in an external strain field. Journal of Turbulence, 3, 37-37.

Carton, X., Meunier, T., Flierl, G.R., Perrot, X., Sokolovsiy, M.A., 2010b: Explosive instability of geostrophic vortices. Part 1. Parametric instability. Theor. Comp. Fluid Dyn., 24, 131-135.

Carton, X., Sokolovskiy, M., Ménesguen, C., Aguiar, A., Meunier, T., 2014. Vortex stability in a multi-layer quasi-geostrophic model: application to Mediterranean Water eddies. Fluid Dynamics Research, 46(6), 061401.

Ciani, D., Carton, X., Verron, J., 2016. On the merger of subsurface isolated vortices. Geophysical & Astrophysical Fluid Dynamics, 110(1), 23-49.

Cohen, Y., Dvorkin, Y., Paldor, N., 2015. Linear instability of constant potential vorticity cold core eddies in a two-layer ocean. Quart. J. Roy. Met. Soc, 141 (692), doi: 10.1002/qj.2575.

Cohen, Y., Dvorkin, Y., Paldor, N., 2016. On the stability of outcropping eddies in a constant ‐ PV ocean. Quart. J. Roy. Met. Soc., 142 (699), doi: 10.1002/qj.2785.

Cushman-Roisin, B., 1986. Frontal geostrophic dynamics. J. Phys. Oceanogr., 16 (1), 132-143.

Cushman-Roisin, B., Beckers, J.M., 2011. Introduction to geophysical fluid dynamics: physical and numerical aspects, Vol. 101, Academic Press, p. 828.

Davey, M.K., 1977. Baroclinic instability in a fluid with three layers. J. Atmos. Sci, 34, 1224-1234.

Dewar, W.K., Killworth, P.D., 1995. On the stability of oceanic rings. J. Phys. Oceanogr., 25, pp. 1467-1487.

Flierl, G.R., 1988. On the instability of geostrophic vortices. J. Fluid Mech. 197, 349–388.

Gascard, J.-C., Mork, K.A., 2008. Climatic importance of large-scale and mesoscale circulation in the Lofoten Basin deduced from Lagrangian observations. Arctic-Subarctic Ocean Fluxes. Defining the Role of the Northern Seas in Climate/ Ed. by Dickson R.R., Meincke J., Rhines P. Springer Science. P. 131-144.

Gryanik, V.M., Sokolovskiy, M.A., Verron J., 2006. Dynamics of heton-like vortices. Regul. Chaotic Dyn. 11(3), 417-438.

Helfrich, K.R., Send, U., 1988. Finite-amplitude evolution of two-layer geostrophic vortices. J. Fluid Mech., 197, 331-348.

Hetland, R. D. (2017). Suppression of Baroclinic Instabilities in Buoyancy-Driven Flow over Sloping Bathymetry. Journal of Physical Oceanography, 47(1), 49-68.

Holmboe, J., 1968. Instability of baroclinic three-layer models of the atmosphere. Geofys. Publ, Universitetsforlaget. Oslo, 27, 1-27.

Hua, B. L., Ménesguen, C., Le Gentil, S., Schopp, R., Marsset, B., Aiki, H., 2013. Layering and turbulence surrounding an anticyclonic oceanic vortex: in situ observations and quasi-geostrophic numerical simulations. J. Fluid Mech., 731, 418-442.

Ikeda, M., 1981. Instability and splitting of mesoscale rings using a two-layer quasi-geostrophic model on an f-plane. J. Phys. Oceanogr., v. 11, pp. 987-998.

Ikeda, M., 1993. Linear instability of a current flowing along a bottom slope using a three-layer model. J. Phys. Oceanogr. 13, 208-223.

Isachsen, P.E., 2015. Baroclinic instability and the mesoscale eddy field around the Lofoten Basin, J. Geophys. Res. 120, 4, 2884-2903.

Ivanov, V.V., Korablev, A.A., 1995a. Formation and regeneration of the pycnocline lens in the Norwegian Sea, [in Russian], Russ. Meteorol. Hydrol., 9, 62–69.

Ivanov, V.V., Korablev, A.A., 1995b. Dynamics of pycnocline lens in the Norwegian sea [in Russian], Russ. Meteorol. Hydrol. 10, 55-62.

Jakobsen, P.K., Ribergaad, M.H., Quadfasel, D., Schmith, T., Hughes, Ch.W., 2003. Near-surface circulation in the northern North Atlantic as inferred from Lagrangian drifters: Variability from the mesoscale to interannual. J. Geophys. Res., 108 (C8). 3251-3264.

Kamenkovich, V.M., Larichev, V.D., Khar'kov, B.V., 1982. A numerical barotropic model for analysis of synoptic eddies in the open ocean. Oceanology, 21 (6), 549-558.

Katsman, G.A., van der Vaart, P.C.F., Dijkstra, H.A., de Ruiter, W.P.M., 2003. Stability of multilayer ocean vortices: a parameter study Including realistic Gulf Stream and Agulhas rings. J. Phys. Oceanogr., v. 33, pp. 1197-1218.

Killworth, P.D., Blundell, J.R., Dewar, W.K., 1997. Primitive equation instability of wide oceanic rings. Part I: Linear theory. J. Phys. Oceanogr., v. 27, pp. 941-962.

Köhl, A., 2007. Generation and stability of a quasi-permanent vortex in the Lofoten Basin. J. Phys. Oceanogr. 37, 2637-2651.

Koszalka I., LaCasce, J.H., Andersson, M., Orvik, K.A., Mauritzen, C., 2011. Surface circulation in the Nordic Seas from clustered drifters. Deep-Sea Research, Part I. 58. P. 468-485. doi:10.1016/j.dsr.2011.01.007.

Kozlov, V.F., Makarov, V.G., Sokolovskiy, M.A., 1986. Numerical model of the baroclinic instability of axially symmetric eddies in two-layer ocean. Izvestiya, Atmos. Ocean. Phys, 22, 674-678.

Lamb, H., 1885. Hydrodynamics, 2nd ed. Cambridge: Cambridge University Press.

Lai, D.Y., Richardson, P.L., 1977. Distribution of movement of Gulf Stream rings. J. Phys. Oceanogr., v. 7, pp. 670-683.

Locarnini, R.A., Mishonov, A.V., Antonov, J.I., Boyer, T.P., Garcia, H.E., Baranova, O.K., Zweng, M.M., Johnson, D.R., 2010. World Ocean Atlas. In: Levitus, S. (Ed.), Temperature Vol. 1. NOAA Atlas NESDIS68, U.S. Government Printing Office, Washington, D.C., p.184.

Losch, M., Menemenlis, D., Heimbach, P., Campin, J.-M., Hill, C., 2010. On the formulation of sea - ice models. Part 1: Effects of different solver implementations and parameterizations. Ocean Model. 33, 129–144.

Lumpkin, R., Johnson, G.C., 2013. Global ocean surface velocities from drifters: mean, variance, ENSO response, and seasonal cycle. J. Geophys. Res. 118, 2992–3006. http://dx.doi.org/10.1002/jgrc.20210.

Mahdinia, M., Hassanzadeh, P., Marcus, P. S., Jiang, C. H., 2016. Stability of 3D Gaussian vortices in rotating stratified Boussinesq flows: Linear analysis. J. Fluid Mech., arXiv preprint arXiv:1605.06859.

Mariotti, A., Legras, B., Dritschel, D.G., 1994. Vortex stripping and the erosion of coherent structures in two-dimensional flows. Physics of Fluids 6 (12), 3954-3962.

Makarov, V.G., Sokolovskiy, M.A., Kizner, Z., 2012. Doubly symmetric finite-core heton equilibria. J. Fluid Mech, 708, 397-417.

Maximenko N.A., Orlov, O.I., 1991. Integral characteristics of the core of quasi-stationary “Gauss” vortex in homogeneous and shear flows. Oceanology 31, 34-41

Marshall, J., Adcroft, A., Hill, C., Perelman, L., Heisey, C., 1997. A finite volume,incompressible Navier–Stokes model for studies of the ocean on parallel computers. J. Geophys. Res. 102, 5753–5766. http://dx.doi.org/10.1029/96JC02775.

Ménesguen, C., Hua, B.L., Carton, X., Klingelhoefer, F., Schnürle, P., Reichert, C., 2012. Arms winding around a meddy seen in seismic reflection data close to the Morocco coastline. Geophysical Research Letters, 39, L05604, doi: 10.1029/2011GL050798.

Mesquita, S.B., Prahalad, Y.S., 1999. Statistical stationary states for a two-layer quasi-geostrophic system. Proc. Indian Acad. Sci. (Math. Sci), 109, 107-115.

Morel, Y., McWilliams, J., 1997. Evolution of isolated interior vortices in the ocean. J. Phys. Oceanogr., v. 27, pp. 727-748.

Nguyen, A.T., Menemenlis, D., Kwok, R., 2011. Arctic ice - ocean simulation with optimized model parameters: approach and assessment. J. Geophys. Res. 116, C04025. http://dx.doi.org/10.1029/2010JC006573.

Nguyen, H.Y., Hua, B.L., Schopp, R., Carton, X., 2012. Slow quasigeostrophic unstable modes of a lens vortex in a continuously stratified flow. Geophysical & Astrophysical Fluid Dynamics, 106(3), 305-319.

Nilsen, J. E. Ø., Falck, E., 2006. Variations of mixed layer properties in the Norwegian Sea for the period 1948–1999. Progress in Oceanography, 70(1), 58-90.

Nilsen, J. E. Ø., Nilsen, F., 2007. The Atlantic Water flow along the Vøring Plateau: Detecting frontal structures in oceanic station time series. Deep Sea Research I, 54(3), 297-319.

Nøst, O.A., Isachsen, P.E., 2003. The large-scale time-mean ocean circulation in the Nordic Seas and Arctic Ocean estimated from simplified dynamics. Journal of Marine Research, 61, P. 175-210.

Nurser, A.J.G., Bacon, S., 2014. The Rossby radius in the Arctic Ocean. Ocean Science, 10(6), 967-975.

Oort, A.H., Ascher, S.C., Levitus, S., Peixóto, J.P., 1989. New estimates of the available potential energy in the world ocean. Journal of Geophysical Research: Oceans, 94(C3), 3187-3200.

Orvik, K.A., 2004. The deepening of the Atlantic water in the Lofoten Basin of the Norwegian Sea, demonstrated by using an active reduced gravity model. Geophys. Research Letters, 31, L01306. doi:10.1029/2003GL018687.

Paldor, N., Nof, D., 1990. Linear instability of an anticyclonic vortex in a two-layer ocean. J. Geophys. Res, 95, 18,075-18,079.

Paldor, N. 1999. Linear instability of barotropic submesoscale coherent vortices observed in the ocean. J. Phys. Oceanogr., 29(7), 1442-1452.

Pedlosky, J., 1985. The instability of continuous heton clouds. J. Atmos. Sci, 42, 1477-1486.

Pedlosky, J., 1987. Geophysical fluid dynamics. Springer Verlag, 710 pp.

Pereskokov, A.I., 1999. On the physical nature of large-scale counter-cyclical cycle in the water column of the Norwegian Sea. Reports of the Academy of Sciences, 364, 4, 549-552.

Poulain, P.-M., Warn-Varnas, A., Niiler, P.P., 1996. Near-surface circulation of the Nordic Seas as measured by Lagrangian drifters. Journal Geophysical Research 101, 18,237–18,258.

Raj, R.P., Chafik, L., Nilsen, J.E.Ø, Eldevik, T., Halo, I., 2015. The Lofoten Vortex of the Nordic Seas. Deep-Sea Research, I96, 1–14.

Reinaud, J.N., Carton, X., 2009. The stability and the nonlinear evolution of quasi-geostrophic hetons. J. Fluid Mech, 636, 109-135.

Richardson, P.L., Bower, A.S., Zenk, W., 2000. A census of Meddies tracked by floats. Progress in Oceanography, 45 (2), 209-250.

Ripa, P., 1992. Instability of a solid-body rotating vortex in a two-layer model. J. Fluid Mech, 242, 395-417.

Romantcev, V.A., 1991. Large-scale structure and characteristics of the average circulation of the water. Problems of the Arctic and Antarctic. Vol. 65. Gidrometeoizdat. P. 75-97.

Rossby, T., Ozhigin, V., Ivshin, V., Bacon, Sh., 2009. An isopycnal view of the Nordic Seas hydrography with focus on properties of the Lofoten Basin. Deep-Sea Research Part I. 2009. 56, (11), 1955-1971.

Skagseth, Ø., Furevik, T., Ingvaldsen, R., Loeng, H., Mork, K. A., Orvik, K. A., & Ozhigin, V. (2008). Volume and heat transports to the Arctic Ocean via the Norwegian and Barents Seas. In Arctic–Subarctic Ocean Fluxes (pp. 45-64). Springer Netherlands.

Smeed, D.A., 1988a. Baroclinic instability of three-layer flows: 1. Linear stability. J. Fluid Mech, 194, 217-231.

Smeed, D.A., 1988b. Baroclinic instability of three-layer flows: 2. Experiments with eddies. J. Fluid Mech, 194, 233-259.

Smith, W.H.F., Sandwell, D.T., 1997. Global sea floor topography from satellite altimetry and ship depth soundings. Science 277 (5334), 1956–1962.

Søiland, H., Prater, M., Rossby, T., 2008. Rigid topographic control of currents in the Nordic Seas. Geophysical Research Letters 35, L18607, doi:10.1029/2008GL034846.

Søiland, H., Rossby, T., 2013. On the structure of the Lofoten Basin Eddy. J. Geophys. Res. Oceans. 118, 4201–4212. http://dx.doi.org/10.1002/jgrc.20301.

Sokolovskiy, M.A., 1988. Numerical modelling of nonlinear instability for axisymmetric two-layer vortices. Izvestiya, Atmos. Ocean. Phys, 24, 536-542.

Sokolovskiy, M.A., 1991. Modeling triple-layer vortical motions in the ocean by the Contour Dynamics Method. Izvestiya, Atmos. Ocean. Phys., 27(5), 380-388.

Sokolovskiy, M.A., 1997a. Stability analysis of the axisymmetric three-layered vortex using contour dynamics method. Comput. Fluid Dyn. J., 6(2), 133-156.

Sokolovskiy, M.A., 1997b. Stability of an axisymmetric three-layer vortex. Izvestiya, Atmos. Ocean. Phys., 33(1), 16-26.

Sokolovskiy, M.A., Verron, J., 2000. Finite-core hetons: Stability and interactions. J. Fluid Mech, 423, 127-154.

Sokolovskiy, M., Verron, J., Carton, X., Gryanik, V., 2010. On instability of elliptical hetons. Theor. Comput. Fluid Dyn, 24, 117-123.

Sokolovskiy, M.A., Verron, J., 2014. Dynamics of vortex structures in a stratified rotating fluid. Series Atmospheric and Oceanographic Sciences Library. Vol. 47, Springer: Cham - Heidelberg - New York - Dordrecht - London.

Spall, M.A., 2010. Dynamics of Downwelling in an Eddy-Resolving Convective Basin. J. Phys. Oceanogr., 40, 2341–2347.doi: http://dx.doi.org/10.1175/2010JPO4465.1

Sutyrin, G., 2015. Why compensated cold-core rings look stable. Geophys. Res. Lett., 42(13), 5395-5402.

Thierry, V., Morel, Y.. 1999. Influence of a strong bottom slope on the evolution of a surface-intensified vortex. J. Phys. Oceanogr., 28, 911–924.

Thivolle-Cazat, E., Sommeria, J., Galmiche, M., 2005. Baroclinic instability of two-layer vortices in laboratory experiments. J. Fluid Mech., 544, 69-97.

Torrence, C., Compo, G.P. 1998. A Practical Guide to Wavelet Analysis. Bulletin of the American Meteorological Society, 79 (1), 61-78.

van Geffen, J.H.G.M., Davies, P.A., 2000. A monopolar vortex encounters an isolated topographic feature on a beta-plane. Dynamics of Atmospheres and Oceans 32 (1), 1-26, doi:10.1016/S0377-0265(99)00040-8.

Volkov, D.L., Belonenko, T.V., Foux, V.R., 2013. Puzzling over the dynamics of the Lofoten Basin - a sub-Arctic hot spot of ocean variability. Geophysical Research Letters. 40, 1–6.

Volkov, D.L., Kubryakov, A.A., Lumpkin, R., 2015. Formation and variability of the Lofoten Basin vortex in a high-resolution ocean model. Deep-Sea Research. I. 105. 142–157.

Wright, D.G., 1980. On the stability of a fluid with specialized density stratification. Part I: Baroclinic instability and constant bottom slope. J. Phys. Oceanogr, 10, 639-666.

Zabusky N.J., Hughes M.H., Roberts K.V., 1979. Contour dynamics for the Euler equations in two dimensions. J. Comput. Phys., 30(1), 96-106.

Figure captions

Fig. 1. Topographic map of the Lofoten Basin (depth in m) with the major flows overlaid. One minute GEBCO topography is used. Gray dashed contours mark 3000 m, gray solid contours – 3200 m and solid black contours – 3250 m depth. Surface and deep currents are sketched with dark red and blue lines, respectively. The magenta dot in the center of the LB is the most frequent position of the Lofoten Vortex (LV). The magenta line around the dot limits the area

where the LV center is observed 80% of time for the 15 years of simulations with MIT GCM. NwASC is the Norwegian Atlantic Slope Current, NwCC is the Norwegian Atlantic Coastal Current.

Fig. 2. A section of salinity (a) and of temperature (°C, b) across the center of the Lofoten Vortex (69.7°N) at 24.08.2005 in the MIT GCM simulations. Thin isolines mark potential density surfaces referenced to 500 m depth. The LV position and the mean depths of the 3 layers used for stability analysis are marked with dashed rectangles. GEBCO topography, interpolated to the model grid, limit the data distribution from below (blue line). Magenta lines mark the frequency of observation of the LV center along this section (out of scale).

Fig. 3. Upper panels: relative vorticity distribution at 100 m depth (x10^{-5} s^{-1}). Red and magenta lines connect the LV centre and the LV boundaries in radial directions. Lower panel: sampled profiles of relative vorticity for the distributions above, running from the LV center northwards. (a) – 10.02.1993; (b) – 08.09.1993; (c) – 11.11.1998. Red ellipse (upper plots) and empty circles (lower plots) mark the LV boundary defined with the first algorithm (as described in the text); dashed magenta ellipse (upper plots) and grey stars (lower plots) mark the boundary defined with the second algorithm (as described in the text).

Fig. 4. Horizontal maps at 100 m depth (left-hand panels) and vertical profiles (middle and right-hand panels) of relative vorticity (x10^{-5} s^{-1}) in the Lofoten Basin: a- 24.08.2005; b- 13.09.2009. In the horizontal maps horizontal velocity vectors are overlaid; black and grey lines mark the position of vertical section along the LV semi-major and semi-minor axes of the approximating ellipse, respectively. The vertical sections show cuts along the semi-major axis (middle panels) and semi-minor axis (right-hand panels) of the vortex. In the vertical sections solid black isolines are $\sigma_{0.5}$ and vertical white dotted and dashed lines mark the LV axis and boundaries (dynamic radii), respectively.

Fig. 5. Vertical profiles of selected time-mean characteristics of the LV (from 1998 to 2012): black lines with circles are dynamic radii (km) – the mean radius (solid line - R_{av}), the lengths of the semi-minor axis (dashed line - $R_{\min}$) and of the semi-major (dotted line - $R_{\max}$) axis; thick grey lines with crosses are relative vorticity profiles (10^6 s^{-1}) – the peak (solid line - ω_{min}) and averaged in the disk with the radius $R_{av}/2$ (dashed line - ω_{av}), thick gray line with squares is the maximum azimuthal velocity (V , cm s^{-1}); black dash-dot line is profile of Ertel potential vorticity anomaly in the LV center (Π_E, 10^{11} s^{-1}). Gray horizontal bands present approximate positions of the time mean upper and lower boundaries of the LV core.

Fig. 6. a - time evolution of the mean layer thicknesses (m) outside the LV: layer 1 (h_1, thick solid red line) and layer 2 (h_2, thick dotted magenta line); time evolution of the LV core thickness (m), - separation between upper and lower interfaces of layer 2 at the LV center ($h_{2\mathrm{LV}}$, thin solid blue line). b - time evolution thickness (m) of layer 1 in the LV center ($h_{1\mathrm{LV}}$, thin solid blue line), and elevation of isopycnals over the LV (m): thick solid red line is η_1, thick dotted magenta line is $|\eta_2|$.

Fig. 7. a- time evolution of layer-mean temperature (°C), b - time evolution of layer-mean density $\sigma_{0.5}$ (kg m^{-3}) in the LV. Red line represents layer 1, magenta line - layer 2; blue line – layer 3.

Fig. 8. (a)- time evolution of layer-mean LV radius (km). (b) - time evolution of maximum azimuthal velocity (cm s^{-1}). (c) - time evolution of the mean relative vorticity within the circle $r \le R_j / 2$ around the LV center (s^{-1}). Red line represents layer 1, magenta line - layer 2; blue line – layer 3.

Fig. 9. (a) - time evolution of the layer-mean QG PV (Eq. (1), s^{-1}) in the LV ($r \le R_j$, j =1,2,3 is the layer number). (b) - time evolution of the layer-mean QG PV (s^{-1}) around the LV ($R_j \le r \le 2\mathrm{R}_j$). Red line represents layer 1, magenta line - layer 2; blue line – layer 3. Note that y-scale of panel (a) is in 10^{-4} s^{-1}, while of panel (b) is in 10^{-5} s^{-1}.

Fig. 10 – The state of the LV in (Π_1, Π_2) space (10^{-4} s^{-1}) and the results of K-mean cluster analysis. (a) Black dots show data points and grey shading indicate their concentration (darker shading indicates higher density). The thicker red, magenta, blue, cyan and green dots represent the (Π_1, Π_2) points identified as belonging to clusters A, B, B1, C, and D, respectively. (b) Number of observations of different states as a function of season over the period of simulations in MIT GCM.

Fig. 11. Mean isopycnal depths (blue lines) across the LV for the four main clusters in Fig. 10. (a) - configuration A, which is the most typical for autumn and early winter, (b) - configuration B, occurring in late winter or early spring, (c) - configuration C, the most typical for late spring, (d) - configuration D, the most typical for summer. Red stars mark the LV limits. Magenta and red lines represent isopycnals, marking the upper and the lower boundaries of the LV core, respectively.

Fig. 12. Same as in Fig. 10 but now with the addition of neutral stability curves based on QG calculations for each of cluster configurations. Colour circles at each of the plates mark the

central set of the corresponding cluster (as in Fig. 10), the dots of the same colour – the rest of the points, belonging to the corresponding cluster. The yellow, red, black and blue are lines of neutral stability curves for azimuthal modes $m=2$, $m=3$, $m=4$ and $m=5$, respectively. (a) the LV PV anomalies (10^{-4} s^{-1}) in (Π_1, Π_2) parameter space for configuration A; (b) the LV PV anomalies (10^{-4} s^{-1}) in (Π_2, Π_3) parameter space for configuration B; (c) the LV PV anomalies (10^{-4} s^{-1}) in (Π_1, Π_2) parameter space for configuration C; (d) the LV PV anomalies (10^{-4} s^{-1}) in (Π_1, Π_2) parameter space for configuration D. The unstable domains of the azimuthal modes are located to the right of the lines with the corresponding labels (in-between the lines of the same mode for (b)). The gray circle in plate (d) marks the PV anomalies of the reference vortex, used for the QG non-linear simulations.

Fig. 13. Evolution of instability in the numerical QG model for small-amplitude $(\varepsilon_j = 0.02, j = 1,2,3)$ mode-2 $(m = 2)$ initial perturbations (see Eq. A.8, Appendix A). The most typical parameter state (Table 1, within configuration D) is used for the model set-up. Each frame shows vortex patches in the upper (red upper contour plots in a plate), middle (magenta middle contour plots in a plate) and lower (blue lower contour plots in a plate) layers as function of non-dimensional time. A dimensionless time unit corresponds to 12 days.

Fig. 14. The same as Fig. 13 but for $m = 3$.

Fig. 15. The same as Fig. 13 but for $m = 4$.

Fig. 16. Evolution of instability in the numerical QG model for finite-amplitude $(\varepsilon_j = 0.2, j = 1,2,3)$ mode-2 $(m = 2)$ initial perturbations (see Eq. A.8, Appendix A). The most typical parameter state (Table 1, within configuration D) is used for the model set-up. Each frame shows vortex patches in the upper (red upper contour plots in a plate), middle (magenta middle contour plots in a plate) and lower (blue lower contour plots in a plate) layers as function of non-dimensional time. A dimensionless time unit corresponds to 12 days.

Fig. 17. The same as Fig. 16 but for $m = 3$.

Fig. 18. The same as Fig. 16 but for $m = 4$.

Fig. 19. The initial state of the QG model with varying topography and the mean flow. The topography presents a set of nested non-concentric cylinders with different depths and radii (marked alternatively with yellow and blue, see text for details). The dashed blue contour presents the 2000 m isobath; with radius of 600 km, it marks the boundary of the Lofoten Basin in the model. Gray contours are the streamlines. Black line marks the separatrix, which limits the area, where particles are not advected out of the simulation region by the mean flow.

Fig. 20. Simulations of the LV evolution in a QG model, when a barotropic background flow and varying bottom topography is approximated with 8 circular non-concentric cylinders with varying plain-depth and radii, and the northeasterly mean flow is added (see Fig. 19 and text for details). The LV is initially centered at the elliptic point of the mean background velocity field. As before, the LV set-up is presented by its most typical parameter state (Table 1, within configuration D). Each frame shows vortex patches in the upper (red upper contour plots in a plate), middle (magenta middle contour plots in a plate) and lower (blue lower contour plots in a plate) layers as function of non-dimensional time. The unperturbed (initial) position of the separatrix is given for reference. The dimensionless time unit corresponds to 12 days.

Fig. 21. As in Fig. 20, but the initial position of the LV is shifted southwestwards, towards the hyperbolic point.

Fig. 22. LV variability in the MIT GCM model at 200 m depth (a-c). In panels (a-c), black, blue and red lines show the variability of perturbations with azimuthal modes 2, 3 and 4, respectively. Panel (a) depicts the normalized perturbations in ring 1 (centered at R_{av}), panel (b) – in ring 2 (centered at 1.5 R_{av}) and panel (c) – in ring 3 (centered at 2 R_{av}). The perturbation intensities are normalized as: $v = (v - v_{4av})/v_{4std}$, where v_{4av} and v_{4std} are time-mean and standard deviation of the perturbation intensity (v) of azimuthal mode 4 in ring 1. Variability of the normalized LV dynamic radius (R_{av}) are shown with green lines. In panels (a-c) LV radius and other parameters below are normalized as: $v = (v - v_{av})/v_{std}$, where v_{av} and v_{std} re time-mean and standard deviation of the corresponding variable. In addition, the following dynamic characteristics of the LV core are shown with cyan lines (for better visibility the lines are centered at y-value 5): panel (a) – normalized absolute value of the relative vorticity of the LV core (ω, averaged within 0.5 R_{av} from the LV center); panel (b) –normalized absolute value of the integral angular momentum (*IAM*, integrated within the circle R_{av}); panel (c) – normalized strain around the LV core (*STR*, mean in the ring $R_{av} \leq r \leq 2R_{av}$). In panel (d) time variations of barotropic potential energy anomaly (PE_s), baroclinic potential energy anomaly (PE_i) and kinetic energy (*KE*), integrated over the LV core volume. The time series are normalized and vertically displaced for better visibility. The LV mergers with other anticyclones are marked with black solid vertical lines. Shaded areas are winter periods of deep mixing.

Fig. 23. Relative vorticity (x10^{-5} s^{-1}, left panels) and vertical velocity (x10^{-2} cm s^{-1}, right panels) at 513 m depth for four consecutive moments of time (a, b, c, d) with the time interval between panel sets of 3 days. White star marks the LV center, grey circle marks the LV dynamic radius,

and grey segment starting at the LV center – the position of maximum of vertical velocity of perturbations of the second azimuthal mode. Black point with white circle and white point with black circle mark a cyclone and an anticyclone in the vicinity of the LV.